Magnetic Continuum Robot with Modular Axial Magnetization: Design, Modeling, Optimization, and Control

Yanfei Cao, *Graduate Student Member*, *IEEE*, Mingxue Cai, *Member*, *IEEE*, Bonan Sun, Zhaoyang Qi, *Graduate Student Member*, *IEEE*, Junnan Xue, *Graduate Student Member*, *IEEE*, Yihang Jiang, Bo Hao, Jiaqi Zhu, Xurui Liu, Chaoyu Yang, and Li Zhang, *Fellow, IEEE*

***Abstract*—Magnetic continuum robots (MCRs) have become popular owing to their inherent advantages of easy miniaturization without requiring complicated transmission structures. The evolution of MCRs, from initial designs with one embedded magnet to current designs with specific magnetization profile configurations (MPCs), has significantly enhanced their dexterity. While much progress has been achieved, the quantitative index-based evaluation of deformability for different MPCs, which can assist in designing MPCs with enhanced robot deformability, has not been addressed before. Here we use "deformability" to describe the capability for body deflection when an MCR forms different global shapes under an external magnetic field. Therefore, in this paper, we propose methodologies to design and control an MCR composed of modular axially magnetized segments. To guide robot MPC design, for the first time, we introduce a quantitative index-based evaluation strategy to analyze and optimize robot deformability. Additionally, a control framework with neural network-based controllers is developed to endow the robot with two control modes: the robot tip position and orientation (M_1) and the global shape (M_2). The excellent performance of the learnt controllers in terms of computation time and accuracy was validated via both simulation and experimental platforms. In the experimental results, the best closed-loop control performance metrics, indicated as the mean absolute errors, were 0.254 mm and 0.626° for mode M_1 and 1.564 mm and 0.086° for mode M_2.**

***Index Terms*—Continuum robots, soft robotics, modular axial magnetization, magnetic actuation, deformability.**

Received 9 July 2024; revised 25 October 2024; accepted 8 December 2024. Date of publication xx xx 2025; date of current version xx xx 2025. This work was supported by the National Key R&D Program of China (Grant No. 2023YFB4705600), in part by National Natural Science Foundation of China (grant No. 62473360), in part by the Shenzhen Science and Technology Program under Grant JCYJ20240813154939050, in part by the Research Impact Fund Project R4015-21, in part by the CUHK internal grants, and in part by the Research Fellow Scheme (project No. RFS2122-4S03) from the Research Grants Council (RGC) of Hong Kong. The authors also thank support from the SIAT-CUHK Joint Laboratory of Robotics and Intelligent Systems, and the Multiscale Medical Robotics Center (MRC), InnoHK, at the Hong Kong Science Park. This article was recommended for publication by Associate Editor xx and Editor Mark Yim upon evaluation of the reviewers' comments. *(Yanfei Cao and Mingxue Cai contribute equally to this work.) (Corresponding author: Li Zhang.)*

Y. Cao is with the Department of Mechanical and Automation Engineering, The Chinese University of Hong Kong, Hong Kong, SAR 999077, China, and also with Shenzhen Research Institute, The Chinese University of Hong Kong, Shenzhen 518000, China.

M. Cai is with the Guangdong Provincial Key Laboratory of Robotics and Intelligent System and the CAS Key Laboratory of Human-Machine Intelligence-Synergic Systems, Shenzhen Institutes of Advanced Technology, Chinese Academy of Sciences, Shenzhen 518000, China.

B. Sun, Z. Qi, J. Xue, Y. Jiang, B. Hao, J. Zhu, X. Liu, and C. Yang are with the Department of Mechanical and Automation Engineering, The Chinese University of Hong Kong, Hong Kong, SAR 999077, China.

L. Zhang is with the Department of Mechanical and Automation Engineering, the Department of Surgery, CUHK T Stone Robotics Institute, and Chow Yuk Ho Technology Centre for Innovative Medicine, The Chinese University of Hong Kong, Hong Kong, SAR 999077, China, with the Multi-Scale Medical Robotics Center, Hong Kong Science Park, Hong Kong, SAR 999077, China, and also with Shenzhen Research Institute, The Chinese University of Hong Kong, Shenzhen 518000, China. (e-mail: lizhang@mae.cuhk.edu.hk)

This article has supplementary downloadable material available at http://doi.org/10.1109/TRO.2024.xxxxxxx, provided by the authors.

Digital Object Identifier 10.1109/TRO.2024.xxxxxxx

I. Introduction

OVER the past few decades, minimally invasive surgery (MIS) has emerged as one of the most notable advancements in the field of surgery. Despite its remarkable merits, such as fewer invasive procedures, decreased pain, and shorter recovery time [1], MIS has challenges such as time-consuming upfront training and rapid fatigue for surgeons [2]. Misoperation caused by the fatigue or physiological stress of surgeons can affect operative accuracy or even trigger MIS failure. Therefore, robotic assistance, particularly robotic systems with high control performance, is essential to alleviating the burden on surgeons and performing accurate operations [3], [4].

Owing to their dexterity potential, continuum robots (CRs) are a solution for robot-assisted surgeries, such as bronchoscopy, neurosurgery, eye surgery, and cardiovascular surgery [5]–[8]. Considerable CRs, functioning as medical guidewires or catheters, are actuated by cables or tendons [9], shape memory alloys [10], [11], pneumatic [12], [13] or hydraulic systems [14], [15], concentric tubes [16], and parallel mechanisms [17]. However, complicated mechanical components are required to endow CRs (except for concentric tubes) with motion transmission capabilities, which impedes their miniaturization to some extent [18].

Compared with the aforementioned actuation methods, magnetic actuation is promising for several aspects: remote and non-contact actuation, easy penetration of biological tissues, and safety for living organisms [19]–[26]. One or more magnets are arranged at the robot tip to endow MCRs with magnetism [27]–[31]. Under a uniform magnetic field, a torque occurs on each magnetic element of the robot when the magnetic moment of the element does not coincide completely with the external field. Therefore, these magnetic elements tend to align themselves with the orientation of the external field to lower the magnetic potential energy. Additionally,

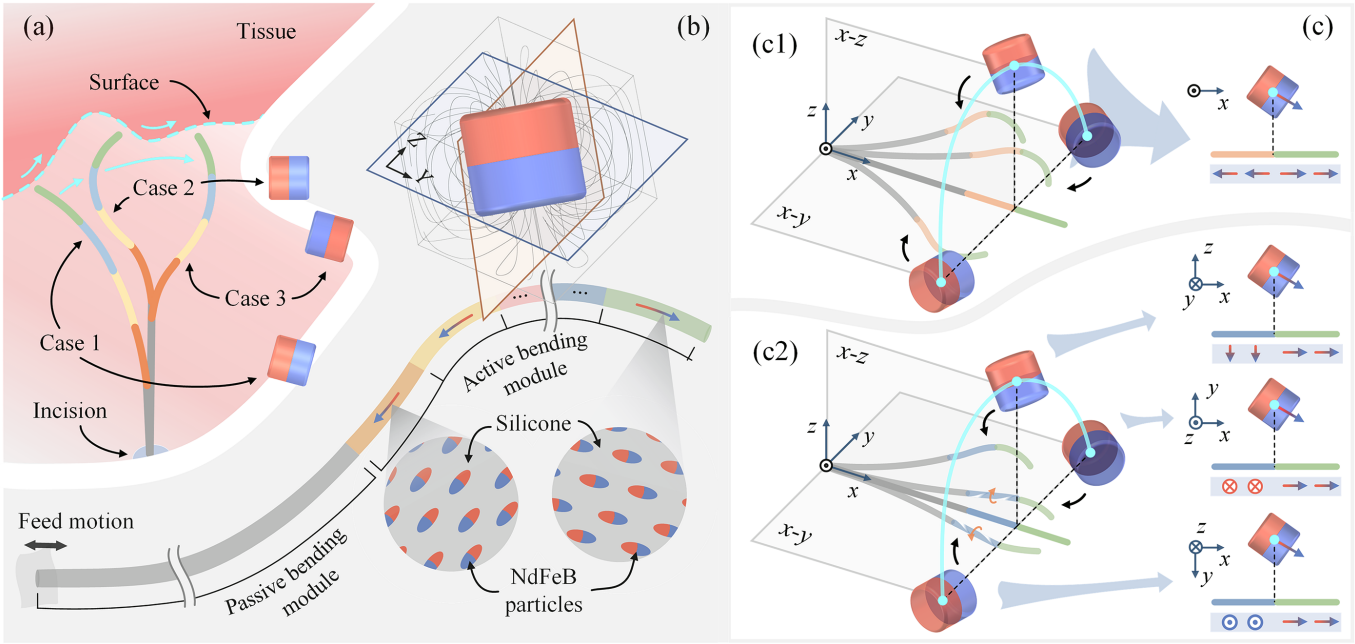

Fig. 1. Conceptual design of the MAMMCR. (a) The robot is expected to navigate and track by adaptively tuning the global shape. This may increase the potential of the robot in some medical applications, such as drug delivery or laser ablation. (b) Conceptual design: the robot body primarily contains two parts: the passive and active bending modules. Specifically, each segment of the active bending module, which contains magnetic silicone (silicone mixed with NdFeB particles), can be selectively magnetized to have different axial magnetization orientations. The modular MPC enables the robot to adaptively deform into different shapes during navigation under the feed motion and magnetic actuation. (c) Magnetism features of two MCRs with non-axial and axial MPCs: (c1) The robot has the same magnetism distribution in different radial directions to show workspace symmetry and potentially benefit the robot magnetic control. (c2) From different radial directions, the magnetism distribution of the robot with a non-axial magnetization profile shows asymmetry.

the robot deformation caused by this alignment increases the elastic potential. The final balanced state appears when the total potential of the system reaches a minimum value. When the field is nonuniform, the magnetic torque and force function together to introduce robot deformation. Owing to the remote actuation, intricate transmission structures are not required for MCRs, enabling robot miniaturization [19], [32], [33]. To further miniaturize MCRs and improve safety, researchers have used magnetic soft materials (silicone or hydrogels mixed with ferromagnetic microparticles) in robot prototypes [34]–[36]. Compared with conventional permanent-magnet robot designs, stronger external fields are required for comparable deformations because magnetic silicone exhibits weaker magnetism than permanent magnets at the same scale.

Although miniaturization is possible, these MCRs lack the level of dexterity of CRs actuated using other methods [19]. MCRs with a traditional one-segment design can hardly achieve dexterous shape deformation decoupling from the tip position or orientation. To enhance the dexterity, researchers have investigated MCRs using magnetization programming technology [37]–[39], [41]–[44]. Tethered MCRs embedded with two oppositely magnetized magnets can achieve different deformation shapes [37], [38], although more permanent magnets in an MCR increase the safety risk of being left in the body when a prototype ruptures [36]. To further improve the dexterity, we first proposed a new concept of intraoperative magnetic moment programming for MCRs actuated by uniform magnetic fields in our previous papers. Different magnetic moment combinations can be obtained during robot navigation using polymer phase-changing technology [39] or shape memory alloy actuation [40], but it results in a complex structural design and time-consuming heating and cooling processes.

Recently, researchers have explored customized and lengthwise distributed MPCs in magnetic silicone MCRs [41]–[44]. Although they lack the capability of intraoperative magnetic moment programming, these MCRs can deform into specific shapes, benefiting from preoperative customized non-axial MPCs [41]. Similarly, theoretical modeling [43], a learnt method [44], and a Jacobian-based controller [45], [46] have been introduced to generate a series of asymmetric MPCs to endow MCRs with time-varying shaping capabilities. These MCRs adopt non-axial MPCs to enhance their deformability. As shown in Fig. 1(c), the non-axial MPC exhibits different magnetism distributions in different radial direction. Although different non-axial magnetization designs have been demonstrated to be suitable for different tasks [41], workspace asymmetry can be observed in Fig. 1(c2). Moreover, the axial MPC causes MCRs to have an identical magnetism distribution in different radial directions, which ensures robot workspace symmetry and potentially facilitates robot control (Fig. 1(c1)). Except for this, from our perspective, a quantitative evaluation of the deformability of different robot MPCs with indices has not yet been addressed. This is crucial for guiding MPC design, particularly for axial MPCs. Although different magnetization combinations in the modular axial MPC can endow a robot with different deformabilities, according to our analysis results, the robot deformability does not intuitively

TABLE I
CONTROL PERFORMANCE OF MAGNETIC CONTINUUM ROBOTS AMONG OUR ROBOT AND TYPICAL PROTOTYPES IN EXISTING WORKS

Reference	Robot body magnetic component	Kinematics method	Controller design	Computation time [ms] (an iteration)	Magnetic actuating method	Body length (estimation) [mm]	Explored range (estimation) [mm^2 or mm^3]	Control mode		Control performance (Mean absolute error)	
								Tip	Shape	Position [mm]	Orientation [°]
[31]	Magnet	Cosserat Rod	Jacobian-based	10	8 EMs	130-170	170×40×40	✔	✗	0.42	—
[48]	Magnet	PRB	Jacobian-based	1.8	6 EMs	∼ 0-70	60×60×60	✔	✗	0.57	—
[30]	Magnet	EBB	Semi-automatic	—	3 EMs	∼ 0-200	200×40×15	✔	✗	1.79	—
[37]	Two magnets	PRB	Jacobian-based	6.5	PM	70-120	100×30×30	✔	✔	1.3	2.8
[45]	NP + Drag (wr = 1:1)	PCC	Jacobian-based	3	2 PMs	40	40×40×40	✔	✔	3.8	—
[47]	NP + Drag (vr = 0.25:1)	—	Learning-based (data from FEM)	—	HC	0-30	20×10	✔	✗	∼ 1	—
Our work*	**NP + Eco (wr = 4:1)**	**PRB**	**Learning-based (data from model)**	**5×10^{-6}**	**PM**	**80-180**	**172×35**	✔	✔	**0.254**	**0.626**

[*] To guide the robot body design, for the first time, we introduced and exploited an index-based evaluation strategy to analyze and optimize the robot deformability. Our learning-based controllers exhibited excellent performances but currently were demonstrated in the plane with gravity counteracted.

[Abbreviations] NP: NdFeB particles; Drag: Dragon Skin 30; Eco: Ecoflex 00-30; wr: weight ratio; vr: volume ratio; EM: electromagnet; PM: permanent magnet; HC: Helmholtz Coil; PRB: pseudo-rigid body; EBB: Euler Bernoulli beam theory; PCC: piecewise constant curvature; FEM: finite element method; ∼: around; —: not support or show this functionality or index.

increase with MPC complexity. Furthermore, an optimized MPC enables accurate robot control and better performance.

To address this, we focus on the design and learning-based control of a modular axially magnetized magnetic continuum robot (MAMMCR)(Fig. 1(b)). The robot is actuated using a robotic arm-based magnetic actuating system (RAMAS). The control performance of our research and latest typical studies on MCRs are compared in Table I. In our work, the optimized axial MPC, obtained from the quantitative deformability evaluation of different magnetization combinations, endowed our robot with a radially isotropic magnetism distribution and good deformability. The control algorithms are developed to achieve accurate two-mode control: the robot tip position and orientation (M_1) and its global shape (M_2). In both simulation and experimental platforms, our robot can navigate and deform with good control performance compared with other robots. This may increase the potential for specific medical applications in body cavities or organs. For example, a robot can be expected to navigate and follow the surface of abdominal tissue or organs while maintaining specific tip orientations to perform drug delivery or laser ablation (Fig. 1(a)). In addition, because of the nitinol core column inside the robot body, the higher stiffness compared with MCRs fabricated from pure soft magnetic silicone might enable the robot to be used in future intracorporeal palpations.

The two main contributions of this study are as follows:

1) To guide the design of robot MPCs, for the first time, we propose a quantitative index-based deformability evaluation strategy. Based on a static pseudo-rigid body (PRB) model of the robot, it is exploited for optimized robot deformability.
2) A control framework with neural network (NN)-based controllers is proposed to achieve high performance in terms of computation time and accuracy. The mean computation time of our learnt controllers during each iteration is $\sim 5 \times 10^{-6}$ ms, which has significant potential for real-time control. The experimental results revealed that the mean absolute errors (MAEs) for the two designed control modes are 0.254 mm and 0.626° for mode M_1 and 1.564 mm and 0.086° for mode M_2.

The remainder of this article is organized as follows: first, the conceptual design and kinematics modeling of the MAMMCR are first discussed in detail. Next, a strategy to quantitatively evaluate the robot deformability is proposed to optimize the robot MPC. Subsequently, we characterize the kinematic behavior of the robot using the optimized MPC. Furthermore, an NN-based control framework is constructed to provide two control modes. Following that, a prototype fabrication method is proposed. Finally, simulation and experimental results confirming the effectiveness of the proposed robot and the corresponding control algorithms are reported.

II. ROBOT CONCEPTUAL DESIGN AND KINEMATICS MODELING

In this section, we design and model the deformation kinematics of the proposed MAMMCR under the actuation of a permanent magnet and feed motion. All symbols, variables, and explanations defined in this section are listed in Table V (Appendix A). The modeling facilitates the optimization of MPCs, deformation behavior characterization, and NN-based control, as described in the next section.

A. Robot Conceptual Design

As shown in Fig. 1(b), the MAMMCR consists of two modules: an active bending module (ABM) and a passive bending module (PBM), which are distributed lengthwise. The ABM contains numerous magnetic segments containing the same magnetic soft material, wherein all segments have the same magnetic dipole intensity but can have different

axial magnetization orientations towards the distal/proximal end of the robot. The PBM is non-magnetic. Consequently, the constructed MPC enables the ABM to form different shapes under a programmable magnetic field. In addition, the feed motion and passive deformation of the PBM, as well as the active deformation of the ABM, are expected to facilitate robot navigation and deformation as desired.

B. Mapping from the Joint Space to Task Space

The navigation and deformation of our robot under the field generated by a permanent magnet exhibit high nonlinearity owing to the continuum characteristic, the nonlinear properties of soft materials, nonlinear magnetic field generated by an external movable magnetic dipole, and highly nonlinear magnetic force and torque on each segment dipole. Thus, we propose approximating robot kinematics as a quasi-static problem. Three main kinematics modeling methods are available for MCRs: the Bernoulli–Euler rod theory [19], [39], Cosserat rod theory [31], and PRB discretization technique [37], [38], [48]. The first two methods can describe the nonlinear variation of continuum curvatures by modeling the mechanics of robot segments, whereas the PRB model approximates the long slender robot body as finite rigid links connected individually via flexible joints to accelerate computations. For the model computation, because the analytical solutions are demanding to be directly given in highly nonlinear MCR kinematic problems, numerical approaches, such as the finite difference method and energy-based method, are leveraged to obtain the appropriate solutions [37]. In our study, we adopt the PRB model coupled with a potential-energy-based approach to model the forward kinematics of an infinite-segment MAMMCR under feed motion and an external magnet dipole.

We first parameterize the configuration of the infinite-segment robot (Fig. 2(a)). Here "infinite" refers to the number of segments that can be magnetized with different magnetization orientations in the ABM. We have a total of $(N_s + 1)\,(N_s \geq 1)$ segments, including one PBM segment (gray) and N_s segments (colors excluding gray) along the MPC of the ABM. We discretize the PBM segment into N_p rigid links, and N_a rigid links are discretized for each ABM segment. All these links are joined individually via flexible and revolute joints. For ease of representation in the modeling, the total $(N + 1)(N = N_p + N_a N_s)$ joints from the proximal end to the distal tip are labeled sequentially as $0, 1, ..., N$. To describe the relationship between these links and joints, we first define a series of reference frames $\{\mathcal{C}_i\}\,(i = 0, 1, ..., N)$. $\{\mathcal{C}_i\}$ adopts the right-hand coordinate form.

We assume that bending and twisting deformations exist in the robot and that the shear and axial extensions are ignored. The link deformation can be described by variable $\boldsymbol{\theta}_i \in \mathbb{R}^3$ (Figs. 2(c) and (d)):

$$\boldsymbol{\theta}_i = \begin{bmatrix}\theta_{i1} & \theta_{i2} & \theta_{i3}\end{bmatrix}^T (i = 1, 2, ..., N) \tag{1}$$

where θ_{i1}, θ_{i2}, and θ_{i3} determine the bending plane, bending angle, and twisting angle of the ith link, respectively, representing the relative pose of reference frame $\{\mathcal{C}_i\}$ with respect to reference frame $\{\mathcal{C}_{i-1}\}$. Thus, the robot deformation angle configuration, that is, the joint space vector of robot $\boldsymbol{\theta} \in \mathbb{R}^{3N}$, is expressed as follows:

$$\boldsymbol{\theta} = \begin{bmatrix}\boldsymbol{\theta}_1^T & \boldsymbol{\theta}_2^T & ... & \boldsymbol{\theta}_N^T\end{bmatrix}^T. \tag{2}$$

To facilitate the following modeling, we specifically denote the reference frame of proximal base $\{\mathcal{C}_0\}$ as $\{\mathcal{B}\}$. For all variables described in $\{\mathcal{B}\}$, the left-hand superscripts denoting the reference frame are omitted for conciseness. Moreover, each reference frame $\{\mathcal{C}_i\}$ is located at the position of the ith flexible joint $\mathbf{p}_i \in \mathbb{R}^3$.

Naturally, the pose of $\{\mathcal{C}_i\}$ with respect to $\{\mathcal{B}\}$ can be described via a homogeneous transformation ${}^{\mathcal{B}}_{\mathcal{C}_i}\mathbf{H}\,(\boldsymbol{\theta}) \in SE(3)$, which can be expressed as the product of exponentials [49]:

$${}^{\mathcal{B}}_{\mathcal{C}_i}\mathbf{H}\,(\boldsymbol{\theta}) = \left[\prod_{j=1}^{i} \exp\left(\sum_{\mathrm{k}=1}^{3} \hat{\boldsymbol{\xi}}_{\mathrm{jk}}\, \theta_{\mathrm{jk}}\right)\right] {}^{\mathcal{B}}_{\mathcal{C}_i}\mathbf{H}_0 \tag{3}$$

where $\hat{\boldsymbol{\xi}}_{jk} \in se(3)$ is the twist at the jth joint. Note that the symbol $\hat{(.)}$ is the mathematical operator representing the mapping from a $\mathbb{R}^6$ (or $\mathbb{R}^3$) vector space to the Lie algebraic space $se(3)$ (or $so(3)$). The twist coordinate $\boldsymbol{\xi}_{jk} \in \mathbb{R}^6$ and corresponding twist $\hat{\boldsymbol{\xi}}_{jk}$ can be described as follows, respectively:

$$\boldsymbol{\xi}_{jk} = \begin{bmatrix}\overline{\boldsymbol{\omega}}_{jk}^T & (-\overline{\boldsymbol{\omega}}_{jk} \times \mathbf{p}_j)^T\end{bmatrix}^T \tag{4}$$

$$\hat{\boldsymbol{\xi}}_{jk} = \begin{bmatrix}\hat{\overline{\boldsymbol{\omega}}}_{jk} & -\overline{\boldsymbol{\omega}}_{jk} \times \mathbf{p}_j \\ \mathbf{O}_{1\times 3} & 0\end{bmatrix} \tag{5}$$

where $\hat{\overline{\boldsymbol{\omega}}}_{jk} \in so(3)$ is the skew-symmetric matrix of unit vector $\overline{\boldsymbol{\omega}}_{jk} \in \mathbb{R}^3$. $\overline{\boldsymbol{\omega}}_{jk}$ denotes the rotation axis of the jth joint: $\overline{\boldsymbol{\omega}}_{j1} = \overline{\boldsymbol{\omega}}_{j3} = \begin{bmatrix}1 & 0 & 0\end{bmatrix}^T$; $\overline{\boldsymbol{\omega}}_{j2} = \begin{bmatrix}0 & 0 & 1\end{bmatrix}^T$. Additionally, ${}^{\mathcal{B}}_{\mathcal{C}_i}\mathbf{H}_0$ interprets the initial pose of $\{\mathcal{C}_i\}$ with respect to $\{\mathcal{B}\}$ without the actuation of the external magnetic field. By combining Eqs. (3)–(5), the position and posture of each robot link can be derived under a determined deformation angle configuration $\boldsymbol{\theta}$. Hence, we complete the derivation of the joint-to-task space mapping $F_{JT}(.)$:

$$\mathbf{t} = F_{JT}(\boldsymbol{\theta}) \tag{6}$$

where $\mathbf{t} \in \mathbb{R}^{5N}$ represents the full task space vector, which can be concretized as

$$\mathbf{t} = \begin{bmatrix}\mathbf{t}_1^T & \mathbf{t}_2^T & ... & \mathbf{t}_N^T\end{bmatrix}^T \tag{7}$$

where $\mathbf{t}_i = \begin{bmatrix}\mathbf{p}_i^T & \boldsymbol{\gamma}_i^T\end{bmatrix}^T \in \mathbb{R}^5$ denotes the state of the ith link, for which $\boldsymbol{\gamma}_{li} = \begin{bmatrix}\gamma_{i1} & \gamma_{i2}\end{bmatrix}^T \in \mathbb{R}^2$ is the link angle vector, and γ_{i1} and γ_{i2} are two angles that describe the tip orientation of the ith link (Fig. 2(c)). Note that the positive and negative signs of the two angles represent counterclockwise and clockwise rotations, respectively. Thus, the position and orientation of each link can be obtained for future numerical analyses and control algorithm designs.

C. Magnetism Parameterization

To model the mapping from the actuation space to the joint space, we must first parameterize the magnetism of

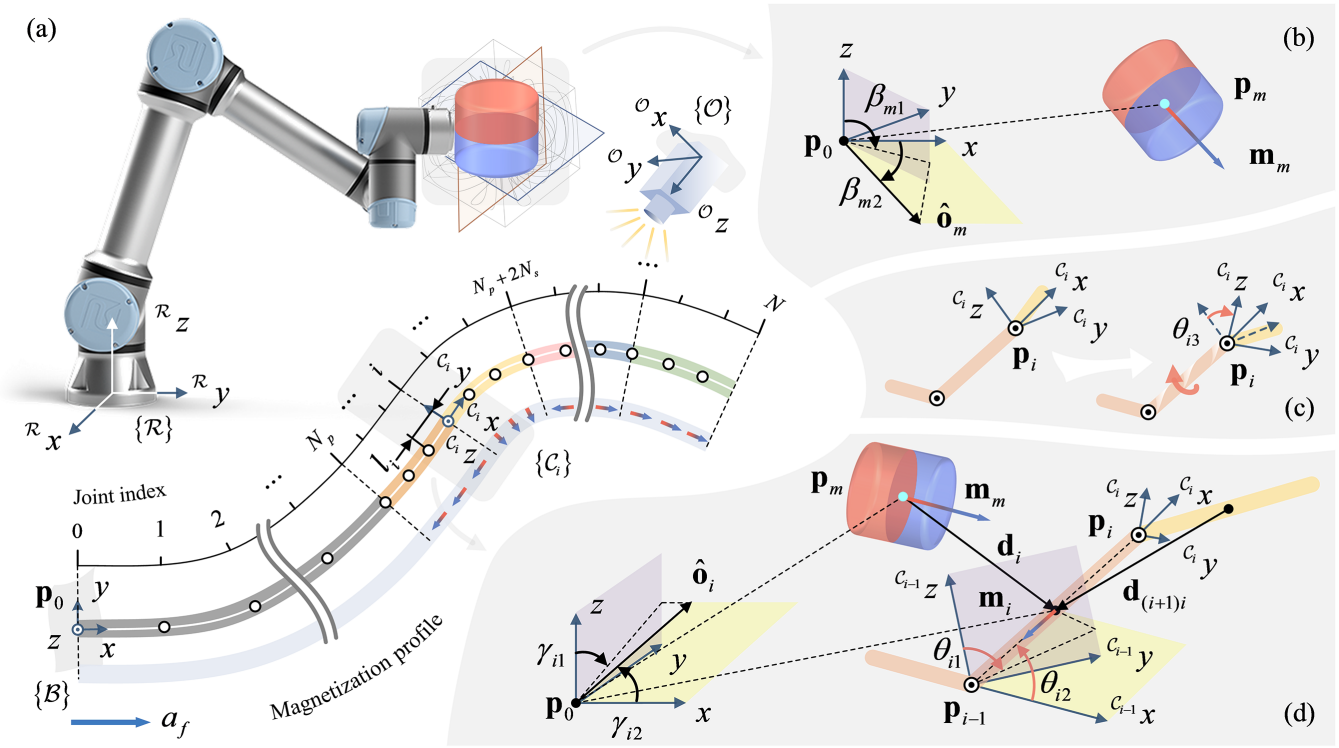

Fig. 2. Kinematics modeling of the robot under the actuation of the feed mechanism and RAMAS. (a) RAMAS employs a 6-DoF robotic arm with the base frame $\{\mathcal{R}\}$ to manipulate a permanent magnet for magnetic field programming. To describe the influence of the generated magnetic field and the feed motion on the robot, the PRB discretization, expressed in the MAMMCR base frame $\{\mathcal{B}\}$, is leveraged to represent the continuous navigation and deformation by connecting N rigid links with the flexible joints. The ith rigid link with the selective magnetization is expressed in its base frame $\{\mathcal{C}_i\}$. The navigation and deformation of the robot is observed in the camera framework $\{\mathcal{O}\}$ for closed-loop feedback. Moreover, the feed motion is discretized into the length increase of each segment in the PBM (grey segments). (b) Modeling of the actuating magnetic dipole with respect to the frame $\{\mathcal{B}\}$. (c) Twisting of the discretized robot link. (d) Geometric description of the ith rigid link of the robot and magnetic interaction between this link and the actuating dipole expressed in the frame $\{\mathcal{B}\}$.

the actuating magnet and each rigid link in the robot. The actuating magnet is approximated as a magnet dipole with a magnetic moment vector $\mathbf{m}_m \in \mathbb{R}^3$:

$$\mathbf{m}_m = m_m \, \overline{\mathbf{o}}_m \tag{8}$$

where $\overline{\mathbf{o}}_m \in \mathbb{R}^3$ is the orientation of the magnetic dipole; m_m represents the strength of $\mathbf{m}_m$, which can be obtained from

$$m_m = (B_r/\mu_0)\, \pi (D_m/2)^2 \, L_m \tag{9}$$

where B_r is the magnet remanence; μ_0 is the vacuum permeability; D_m and L_m are the diameter and length of the actuating magnet, respectively.

To describe the robot magnetism, we must discretize the MPC based on each link of the ABM. Regarding the structure and material of the robot, the segments of the PBM and ABM are connected using a nitinol wire passing through them. In addition, a layer of magnetic silicone exists outside the nitinol wire of the ABM, which endows the ABM with magnetism to actively deform under an external magnetic field. The magnetic moment vector of the ith link $\mathbf{m}_i \in \mathbb{R}^3$ is given by

$$\mathbf{m}_i = m_i \, {}^{\mathcal{B}}_{\mathcal{C}_i}\mathbf{R} \, \overline{\mathbf{w}}_i \tag{10}$$

where m_i is the strength of $\mathbf{m}_i$, which can be derived from

$$m_i = \begin{cases} 0 & (i = 1, 2, ..., N_p) \\ \chi \, \rho_{ms} \, \pi \left[(D_a/2)^2 - (D_p/2)^2 \right] l_i \, m_p & (i = N_p + 1, ..., N) \end{cases} \tag{11}$$

where χ is the mass ratio of magnetic particles in the magnetic silicone; D_a and D_p are the diameters of the ABM and PBM, respectively; l_i is the length of the ith link; m_p is the magnetic moment strength of the magnetic particles per unit mass; ρ_{ms} is the density of the magnetic silicone, which can be estimated using

$$\rho_{ms} = (\rho_p + \rho_s) / \left[\rho_p \, (1 - \chi) + \rho_s \, \chi \right] \tag{12}$$

where ρ_p and ρ_s are the densities of magnetic particles and silicone, respectively; ${}^{\mathcal{B}}_{\mathcal{C}_i}\mathbf{R} \in SO(3)$ is the rotation matrix, which describes the ith link orientation $\overline{\mathbf{o}}_i \in \mathbb{R}^3$; $\overline{\mathbf{w}}_i \in \mathbb{R}^3$ is the unit vector describing the ith link magnetization orientation. Here, we denote the entire MPC of the robot as $\mathbf{W} \in \mathbb{R}^{1\times 3N}$:

$$\mathbf{W} = \begin{bmatrix} \overline{\mathbf{w}}_1^T & \overline{\mathbf{w}}_2^T & \dots & \overline{\mathbf{w}}_N^T \end{bmatrix}. \tag{13}$$

D. Mapping from the Actuation Space to Joint Space

Here, we denote the relationship between the robot deformation angle configuration $\boldsymbol{\theta}$ and the actuating vector $\mathbf{a} \in \mathbb{R}^6$.

TABLE II
GEOMETRIC AND PHYSICAL PARAMETERS IN NUMERICAL SIMULATIONS

Notation	Brief description	Value [Unit]
N_s	Segment number of ABM	4
N_p	Link number of PBM	3
N_a	Link number of ABM segment	3
L_s	Length of ABM	80 [mm]
B_r	Remanence of NdFeB (N52 grade)	1.4 [T]
μ_0	Vacuum permeability	$4\pi \times 10^{-7}$ [T · m/A]
D_m	Diameter of magnet	68 [mm]
L_m	Length of magnet	62.4 [mm]
χ	Mass ratio of magnetic particles	0.8
D_a	Diameter of ABM	2 [mm]
D_p	Diameter of PBM	0.2 [mm]
m_p	Unit magnetic moment of particles	80.68 [emu/g]
ρ_p	Density of particles	7450 [kg/m^3]
ρ_s	Density of silicone (Ecoflex 00-30)	1070 [kg/m^3]

Actuation-to-joint space mapping $F_{AJ}(.)$ is denoted as

$$\boldsymbol{\theta} = F_{AJ}(\mathbf{a}) \tag{14}$$

where the vector $\mathbf{a}$ can be described as follows, including the feed motion a_f and magnetic actuating vector $\mathbf{a}_m \in \mathbb{R}^5$:

$$\mathbf{a} = \begin{bmatrix} a_f & \mathbf{a}_m^T \end{bmatrix}^T \tag{15}$$

where $\mathbf{a}_m = \begin{bmatrix} \mathbf{p}_m^T & \boldsymbol{\beta}_m^T \end{bmatrix}^T$ contains the magnet dipole position $\mathbf{p}_m \in \mathbb{R}^3$, and the angle vector $\boldsymbol{\beta}_m = \begin{bmatrix} \beta_{m1} & \beta_{m2} \end{bmatrix}^T \in \mathbb{R}^2$, where β_{m1} and β_{m2} are the angle swept by rotating from the z axis of $\{\mathcal{B}\}$ to $\overline{\mathbf{o}}_m$ and the angle swept by rotating from the x axis of $\{\mathcal{B}\}$ to the vector obtained by projecting $\overline{\mathbf{o}}_m$ onto the x-y plane, respectively. Note that $\boldsymbol{\beta}_m$ can be mapped from the magnet orientation $\overline{\mathbf{o}}_m$.

First, the magnetic field $\mathbf{B}_i \in \mathbb{R}^3$ exerted on the ith robot link by the actuating magnet, and all magnetic segments are modeled using the magnet dipole model [41]:

$$\begin{aligned} \mathbf{B}_i = \quad & \mu_0/(4\pi \left\|\mathbf{d}_i\right\|^3) \left(3\overline{\mathbf{d}}_i \cdot \overline{\mathbf{d}}_i^T - \mathbf{I}_3\right) \cdot \mathbf{m}_m \\ & + \sum_{j=1}^{N} \left[\mu_0/(4\pi \left\|\mathbf{d}_{ji}\right\|^3) \left(3\overline{\mathbf{d}}_{ji} \cdot \overline{\mathbf{d}}_{ji}^T - \mathbf{I}_3\right) \cdot \mathbf{m}_j\right] \end{aligned} \tag{16}$$

where μ_0 is the vacuum permeability; $\mathbf{d}_i \in \mathbb{R}^3$ and $\mathbf{d}_{ji} \in \mathbb{R}^3$ are the vector from the magnet position $\mathbf{p}_m$ to the geometrical center of the ith link, and the vector from the center of the jth link to that of the ith link, respectively.

Subsequently, we employ numerical methods to locate the point of minimum potential energy to determine the quasi-static equilibrium position of the robot. We estimate the joint configuration $\boldsymbol{\theta}$ corresponding to the given actuation space $\mathbf{a}$. This process can be formulated as a constrained optimization problem as

$$\begin{aligned} & \min_{\boldsymbol{\theta}} \left(V_E + V_B + V_G\right) \\ & s.t. \begin{cases} V_E = \sum_{i=1}^{N} (K_i\, \theta_{i2}^2 + T_i\, \theta_{i3}^2)/2 \\ V_B = -\sum_{i=N_p+1}^{N} \mathbf{m}_i \cdot \mathbf{B}_i \\ V_G = \sum_{i=1}^{N} G_i\, \boldsymbol{\lambda}_{\boldsymbol{z}}\, (\mathbf{p}_i + \mathbf{p}_{i-1})/2 \end{cases} \end{aligned} \tag{17}$$

where V_E, V_B, and V_G are the strain, magnetic potential, and gravitational potential energies of the robot, respectively; K_i and T_i are the bending and torsional stiffnesses of the ith link, respectively; $\boldsymbol{\lambda}_z = \begin{bmatrix} 0 & 0 & 1 \end{bmatrix}$ aids in extracting the coordinate value in the z-direction of the ith link center; G_i is the gravity of the ith link.

III. NUMERICAL SIMULATION

Building on the modeling of robot kinematics introduced above, we propose a quantitative index-based deformability evaluation strategy to study the impact of different MPCs on robot deformability, thus guiding the MPC design of the robot. Subsequently, a deformation behavior characterization of the robot with the optimized MPC is provided to facilitate the control algorithm design in the next section. The parameters used in this section are listed in Table II.

A. Magnetization Profile Optimization

The complicated MPC endows the robot with the ability to deform into complex shapes under simple external magnetic conditions. However, note that this does not mean that increasing the complexity of the magnetization profile is always advisable. Although higher-order deformation shapes can be obtained with a complicatedly designed MPC, the deformation of each segment might decrease correspondingly owing to the mutual constraints of adjacent segments. Thus, we focus on introducing a deformability evaluation scheme to determine the optimized MPC for a five-segment ($N_s = 4$) MAMMCR. Three links exist in each robot segment ($N_a = N_p = 3$). With the optimized profile, the robot is expected to have good deformability for shaping into second- or third-order curves under the combined actuation of a feed mechanism and an external magnet.

As shown in Fig. 3(a), first, we compare the deformation curves of MCRs with the axial MPC (1) and non-axial MPCs (2–5). In this paper, the axes of the magnet and initial-state robot overlap to effectively leverage the actuating magnetic field during actuation. That is, it is advisable for the magnet to move and rotate in the robot bending plane because the axial magnetic field of the actuating dipole is stronger than that in other directions. Thus, the magnet can actuate at a relatively large and safe distance. From the results in Figs. 3(a3)–(a5), robot 1 can maintain the same deformation to ensure workspace symmetry when the magnet rotates. However, robots 2–5 cannot maintain the shapes when the

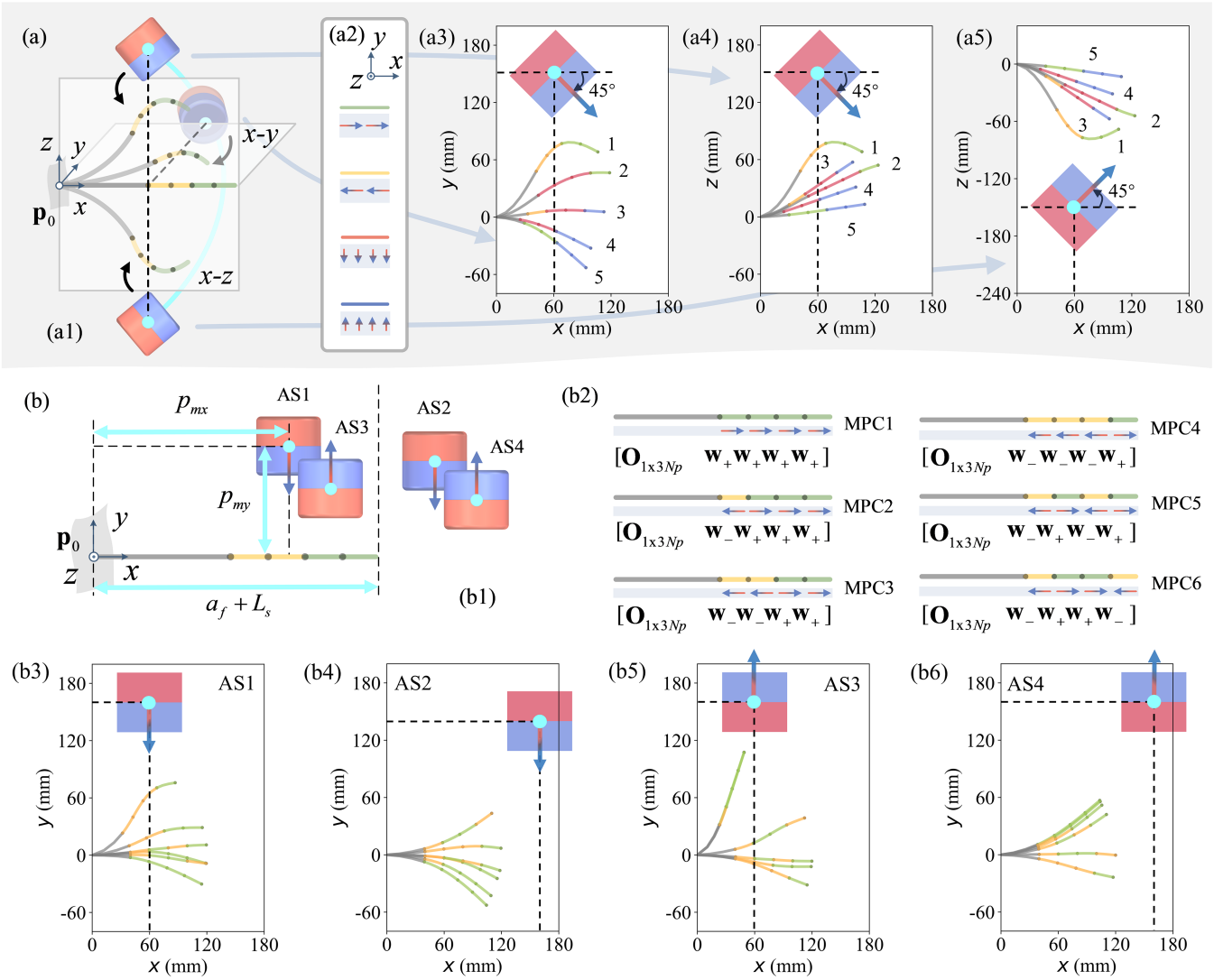

Fig. 3. Deformation curves of the MAMMCR and non-axial magnetized MCRs. (a) Deformation comparison of an MAMMCR and four MCRs with different non-axial MPCs: (a1) Magnet rotates around the x axis to actuate these MCRs. (a2) Legend describes the magnetization orientations of differently colored segments. (a3)–(a5) Deformation curves of these MCRs under three magnetic actuating scenarios. MAMMCR (1) can maintain the same deformation to show workspace symmetry when the magnet rotates; MCRs with non-axial MPCs (2–5) cannot hold the unchanged shapes. (b) Deformation comparison of MAMMCRs with different axial MPCs: (b1) Four typical actuating scenarios AS1–AS4. (b2) Six axial MPCs. (b3)–(b6) Deformation curves of MAMMCRs with the six MPCs. Here, the feed motion $a_f = 40$ mm. The magnet position and orientation are highlighted in each subgraph.

magnet rotates. Subsequently, we determine the optimal axial MPC for the robot. Segments magnetized towards $+/-x$ axis have the magnetizations as $\mathbf{w}_+$ or $\mathbf{w}_- \in \mathbb{R}^{1\times 3N_a}$:

$$\begin{cases} \mathbf{w}_+ = \begin{bmatrix} 1 & 0 & 0 & 1 & 0 & 0 & ... \end{bmatrix} \\ \mathbf{w}_- = \begin{bmatrix} -1 & 0 & 0 & -1 & 0 & 0 & ... \end{bmatrix} \end{cases}. \tag{18}$$

Six different axial MPCs are concretized here (Fig. 3(b2)), which are denoted as MPC1 to MPC6, respectively. Considering the configuration symmetry, the other MPCs not listed here can be made equivalent to one of these six configurations by actuating the magnet with an opposite orientation. For example, configuration $\mathbf{W} = \begin{bmatrix} \mathbf{O}_{1\times 3N_p} & \mathbf{w}_- & \mathbf{w}_- & \mathbf{w}_- & \mathbf{w}_- \end{bmatrix}$ is equivalent to MPC1.

We then analyze the deformability differences among robots with the six aforementioned axial MPCs (Fig. 3(b)). We specify four scenarios, denoted as AS1 to AS4, to typically represent the magnetic actuation of the robots. The magnet of AS1 or AS3 (left side of $x = a_f + L_s$) significantly affects the deformations of both the green and yellow segments, whereas for AS2 or AS4 (right side of $x = a_f + L_s$), the magnet exerts less magnetic influence on the yellow segments (Fig. 3(b1)). Note that although we address the robot deformations in the x-y plane, it is similar to 3D deformations simply by moving or rotating the magnet in 3D space because our modeling is applicable in 3D. The robot deformation curves are shown in Figs. 3(b3)–(b6) and Supplementary Fig. S1. In this analysis, for each of the four scenarios, the magnet maintains its posture while synchronously translating along $+x$ with the advancement of the robot over a distance of 20–60 mm. The robot with MPC1 or MPC2 can almost only maintain C shapes; the robot with MPC4 can only deform into S shapes; the robot

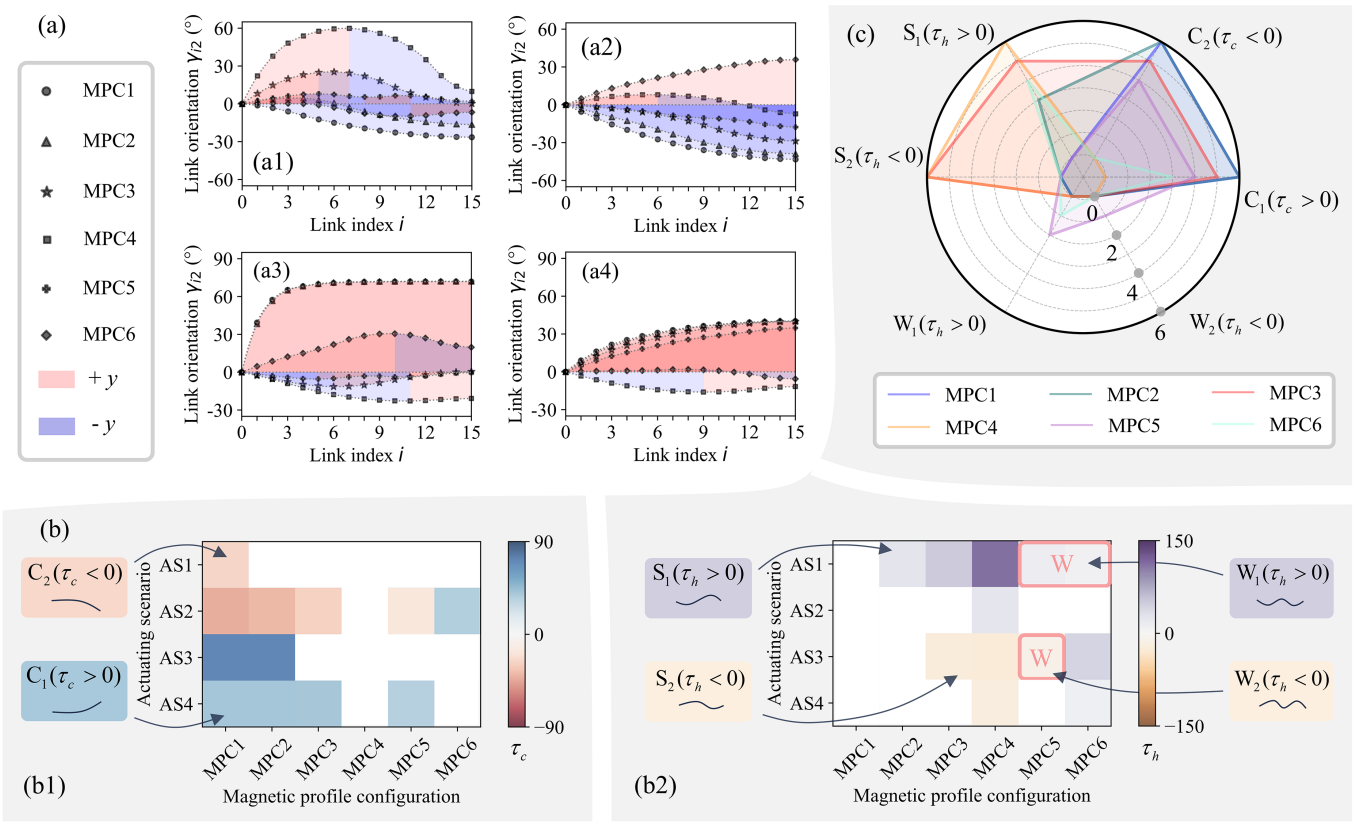

Fig. 4. Deformability analysis of MAMMCRs with different axial MPCs. (a) Deformation angle analysis of robots with MPC1–MPC6: (a1)–(a4) Deformation angles of each robot link under four actuating scenarios AS1–AS4. Here, the feed motion $a_f = 40$ mm. Note that the enclosed region being totally blue or red represents the C-shape deformation; otherwise, the robot deforms into S or higher-order shapes. (b) Deformability analysis of six robots under four actuating scenarios: (b1) Deformability index τ_c analysis. The blue or red region indicates the deformation shape C_1 or C_2. (b2) Deformability index τ_h analysis. Note that in addition to the S-shape deformations, several elements exhibit the higher-order shapes (labeled in red squares). The purple region indicates the deformation shape S_1 or W_1; the orange region indicates the deformation shape S_2 or W_2. Moreover, the darker the element color, the higher the deformability, and vice versa. (c) Ranking of the robots with different axial MPCs in terms of six dimensions. The results show that the robot with MPC3 exhibits relatively higher deformability than other MPCs.

with MPC5 or MPC6 tends to stay in higher-order shapes but with slight deformations; however, the robot with MPC3 can switch between C and S shapes.

To study the deformability of the robot with these six MPCs intuitively, we record the link angles along the MPC during deformations. In the four scenarios, the ith link angle γ_{i1} and γ_{i2} can be obtained:

$$\begin{cases} \gamma_{i1} = 0 \\ \gamma_{i2} = \sum_{k=1}^{i} \theta_{k2} \end{cases} \quad (i = 1, 2, ..., N) \ . \tag{19}$$

The results are shown in Fig. 4(a) and Supplementary Fig. S2. The red and blue regions indicate that the robot link deforms towards $+y$ and $-y$, respectively. A completely enclosed blue or red region indicates a C-shaped robot; an enclosed region containing two or more color sections suggests that the robot maintains an S or higher-order shape. Note that the larger the enclosed region, the greater the deformability of the robot.

Because the total 24 global shapes in Fig. 4(a) can be divided into two main shapes, C (12) and S (9), and a non-dominant shape, W (3), we define two deformability indices: τ_c evaluates deformability when the robot deforms into a C shape; τ_h measures deformability when the robot deforms into an S or higher-order shape. Furthermore, we formulate the two deformability indices:

$$\begin{cases} \tau_c = \gamma_{N2} \\ \tau_h = 2\gamma_{i_p 2} - \gamma_{N2} \end{cases} . \tag{20}$$

Here, τ_c is formulated by the tip link angle γ_{N2} in that the tip orientation can derive the global body of a C-shape robot with a determined feed motion a_f. To reasonably evaluate the global S or W shape with an additional turning point, τ_h is obtained by evaluating the deformations of the two parts divided by the i_pth joint, where the link angle reaches the first non-zero extremum value. Note that positive and negative signs for τ_c indicate the C_1 and C_2 deformations, respectively. Similar to τ_h, the positive value reflects S_1 or W_1 shape, and the negative value reflects S_2 or W_2 (Fig. 4(b)).

Subsequently, we analyze τ_c and τ_h of robots with different MPCs under AS1–AS4. The results are shown in Figs. 4(b1)–(b2) and Supplementary Fig. S3. The darker the color of the element, the better the deformability of the robot. Based on the results, we rank the deformability of these robots in descending order in terms of the six dimensions.

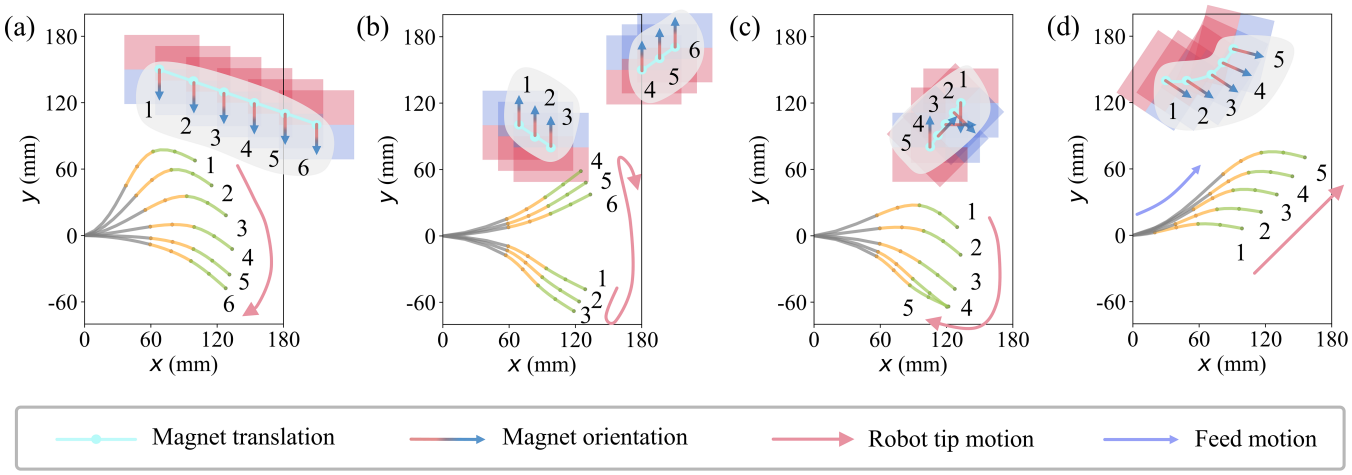

Fig. 5. Deformation behavior characterization of the robot with MPC3 under the actuation of a permanent magnet and the feed mechanism. (a)–(b) Deformation curves under the magnet translation. (a) Robot shape transitions from S_1 (1–4) to C_2 (5–6). Here the feed motion $a_f = 60$ mm. (b) Robot deforms from S_2 (1–3) to C_1 (4–6). However, this translation exhibits snapping (3–4) owing to the pure translation of the magnet without rotation. Here, the feed motion $a_f = 60$ mm. (c) Deformation curves under the magnet translation and rotation. The robot can smoothly transitions from S_1 (1–2), to C_2 (3), and then to S_2 (4–5). Here, the feed motion $a_f = 60$ mm. (d) Deformation curves under the magnet translation, rotation, and the feed motion. The robot can advance with a stable tip posture. Here, the feed motion a_f increases from 20 to 100 mm in 20-mm intervals (1–5). The magnet position and orientation are highlighted in each subgraph.

Each dimension is divided into levels ranging from 6 to 0, where 6 represents the highest and 0 indicates that the robot cannot form specific shapes. The details are shown in Fig. 4(c). Robots with MPC1 and MPC2 perform excellently for C_1 and C_2 while exhibiting a lack of deformability in S_1 and S_2. Robots with MPC4 exhibit outstanding performance for S_1 and S_2 but incompetence for C_1 or C_2. MPC5 and MPC6 enable the robot to deform into higher-older shapes (W_1 and W_2); however, the deformations are very weak. The robots with MPC3 demonstrate a relatively impressive performance across the four dimensions of the upper half-circle. This indicates the potential of the robot with MPC3 to control its tip position, orientation, or global shape during navigation. In addition, although MPC5 and MPC6 have more complicated magnetizations, their deformability indices appear to be inferior in terms of τ_c and τ_h. Hence, we use MPC3 in our robot for subsequent studies.

B. Deformation Behavior Characterization

For an MAMMCR with MPC3, the deformations under the translation and rotation of a magnet and feed motion can be qualitatively analyzed using Eqs. (3), (8), (10), and (17). For the magnet translation, when the magnet orienting $-y$ translates from 1 to 6, the robot shape continuously transitions from S_1 to C_2 (Fig. 5(a)). Under the translation of the magnet orienting $+y$, the robot deforms from S_2 to C_1 but with a snapping (Fig. 5(b)). This transition can be smoothed via the magnet rotation along with the translation. As shown in Fig. 5(c), the robot deformation smoothly changes from S_1, to C_2, and then to S_2. Moreover, when the feed motion is provided along with the combined magnet translation and rotation, the robot advances with a stable tip posture (Fig. 5(d)). These results demonstrate the potential for further accurate control of the robot tip position, orientation, and global shape under the combined actuation of magnet translation, rotation, and feed motion.

IV. Control Framework

Using the optimized MAMMCR, two control modes are developed to control the tip position, orientation, and global shape of the robot. The entire control framework (Fig. 6(a) and Algorithm 1) is constructed in an end-to-end fashion, primarily including the actuating system, MAMMCR, and corresponding software architecture with vision-based closed-loop control algorithms.

A. Control Mode Design

First, to relate the MAMMCR kinematics modeling to the entire system, primarily consisting of the RAMAS for magnetic actuation and the camera for vision-based robot state feedback, we define two coordinates: $\{\mathcal{R}\}$ and $\{\mathcal{O}\}$ are the bases of the RAMAS and camera, respectively (Fig. 2).

Two control modes are designed to enhance the functionality and validate the deformability of the proposed robot. Note that the robot deformations are in the x-y plane, as mentioned previously. The first mode controls the tip position and orientation of the robot. A sequence of robot states $\mathbf{S}^*$ is defined and obtained from the trajectory planning, which can be described as

$$\mathbf{S}^* = [\mathbf{s}_1^{*T} \quad \mathbf{s}_2^{*T} \quad \dots \quad \mathbf{s}_j^{*T} \quad \dots]^T \tag{21}$$

where $\mathbf{s}_j^*$ represents the jth ground truth of a desired sequence $\mathbf{S}^*$. Next, an iterative scheme is employed to make the robot state converges to the desired $\mathbf{s}_j^*$. The real robot state $\mathbf{s}_j(k) \in \mathbb{R}^3$ at time step k is defined as follows:

$$\mathbf{s}_j(k) = [p_{Nx}(k),\ p_{Ny}(k),\ \gamma_{N2}(k)]^T \tag{22}$$

where $p_{Nx}(k)$ and $p_{Ny}(k)$ represent the tip positions, which are the projections of $\mathbf{p}_N(k)$ onto the x- and y-axes of $\{\mathcal{B}\}$,

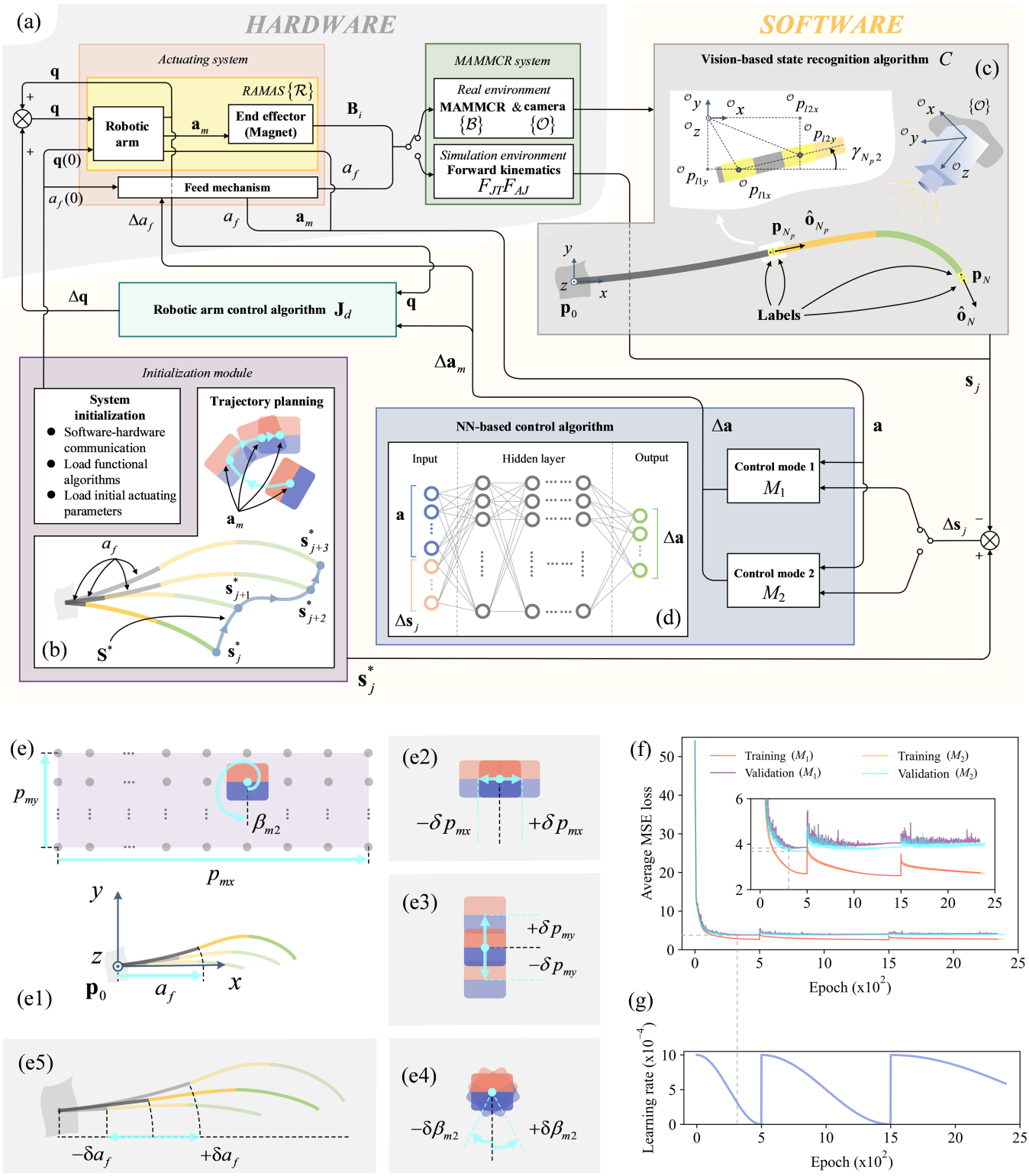

Fig. 6. Architecture of the MAMMCR robot system. (a) Robot control framework to achieve two-mode control in both simulation and real platforms. The hardware part primarily contains the actuating system, including the RAMAS and feed mechanism and MAMMCR. In the real platform, the MAMMCR states are perceived using a camera, whereas in simulation, they are derived from the forward kinematics modeling. The software part primarily contains (b) the initialization module, (c) the vision-based state recognition algorithm, (d) the NN based control algorithm, and the robotic arm control algorithm. (e) Strategy of the data exploration for the NN training: (e1) Sampling of the actuating parameters, including p_{mx}, p_{my}, β_{m2}, and a_f. (e2)–(e5) For each actuating parameter, we give fluctuations to detect how the positive and negative variations of each parameter influence the robot behavior. (f) Average MSE loss curves of the NN trainings. (g) Learning rate curves of the NN trainings. Specifically, the strategy of the cosine annealing with warm starts is used here.

Algorithm 1: NN-Based control of the system

Input: $\mathbf{S}^*$, $\mathbf{a}(0)$

Output: **S**, **A**, **Err** ▷ S, A, and Err saves the states, actuating info, and errors during iterations.

$\mathbf{A}(0) \leftarrow \mathbf{a}(0)$
for $j \leftarrow$ *0 to len*($\mathbf{S}^*$) **do**
  ▷ Set $k_{max} = 300$ as the maximum iteration number.
  for $k \leftarrow$ *0 to* k_{max} **do**
    if k *is 0* **then**
      ▷ Initialize the actuating parameters.
      $\mathbf{a}(k) = \mathbf{A}(-1)$
    end
    if *current_env is simulation_env* **then**
      $\mathbf{s}_j(k+1) \leftarrow F_{JT}(F_{AJ}(\mathbf{a}(k) + \Delta\mathbf{a}(k+1)))$
    else if *current_env is real_env* **then**
      ▷ Observe four markers ($i = 1, 2, 3, 4$) and convert into the controlled state.
      ${}^{\mathcal{O}}\mathbf{s}_j(k+1) \leftarrow C({}^{\mathcal{O}}p_{lix}(k+1), {}^{\mathcal{O}}p_{liy}(k+1))$
      $\mathbf{s}_j(k+1) \leftarrow {}^{\mathcal{B}}_{\mathcal{O}}\mathbf{H}\ {}^{\mathcal{O}}_{j}\mathbf{s}(k+1)$
    end
    $\Delta\mathbf{s}_j(k+1) \leftarrow \mathbf{s}_j^* - \mathbf{s}_j(k)$
    err = MSE($\Delta\mathbf{s}_j(k+1)$)
    $\mathbf{Err}.append(err)$
    if $err \leq \varepsilon$ **then**
      ▷ Set $\varepsilon = 0.25$ as the accuracy threshold.
      $\mathbf{S}(j) \leftarrow \mathbf{s}_j(k)$
      continue
    end
    $\Delta\mathbf{a}(k) \leftarrow M_n(\mathbf{a}(k), \Delta\mathbf{s}_j(k))$
    ▷ Two modes: n= 1, 2.
    $\mathbf{a}(k+1) \leftarrow \mathbf{a}(k) + \Delta\mathbf{a}(k+1)$
    $\mathbf{A}.append(\mathbf{a}(k+1))$
    if *current_env is real_env* **then**
      ▷ Input the actuating increments into the RAMAS and the feed mechanism.
      $\Delta\mathbf{q}(k+1) = \mathbf{J}_d(k)\ {}^{\mathcal{R}}_{\mathcal{B}}\mathbf{H}\ \Delta\mathbf{a}_m(k+1)$
      $q(k+1) \leftarrow q(k) + \Delta\mathbf{q}(k+1)$
      $a_f(k+1) \leftarrow a_f(k) + \Delta a_f(k+1)$
    end
  end
end
return S, **A**, **Err**

respectively. The control objective is to generate an actuation increment $\Delta\mathbf{a}(k+1) \in \mathbb{R}^6$ for a desired state increment $\Delta\mathbf{s}_j(k+1) = \mathbf{s}_j^* - \mathbf{s}_j(k) \in \mathbb{R}^3$ when the robot is in a determined state under the current actuation $\mathbf{a}(k)$. Thus, the control mapping for the first mode M_1 can be expressed as

$$\Delta\mathbf{a}(k+1) = M_1(\mathbf{a}(k), \Delta\mathbf{s}_j(k+1)). \tag{23}$$

To further achieve the control of magnetic actuation via the RAMAS, the joint increment vector $\Delta\mathbf{q}(k+1) \in \mathbb{R}^6$ of a 6-degree-of-freedom (DoF) robotic arm can be mapped from the actuation increment in terms of magnet $\Delta\mathbf{a}_m(k+1)$ as

$$\Delta\mathbf{q}(k+1) = \mathbf{J}_d(k)\ {}^{\mathcal{R}}_{\mathcal{B}}\mathbf{H}\ \Delta\mathbf{a}_m(k+1). \tag{24}$$

We construct the damped Jacobian $\mathbf{J}_d = \mathbf{J}^T(\mathbf{J}\mathbf{J}^T + \boldsymbol{\lambda}_d)^{-1}$ to help avoid divergent behaviors of the robotic arm near singularities [37]. $\mathbf{J} = \partial\mathbf{a}_m/\partial\mathbf{q} \in \mathbb{R}^{5\times6}$ is the calculated Jacobian, and $\boldsymbol{\lambda}_d = \mathrm{diag}(\lambda_1^2\ \mathbf{I}_3, \lambda_2^2\ \mathbf{I}_2)$ is the damping coefficient matrix. Note that λ_1 and λ_2 are two damping coefficients for the magnet position and orientation. In this work, λ_1 and λ_2 are set to be 6×10^{-2} and 6×10^{-3} to obtain the solution with a good convergence speed.

Subsequently, by inputting $\Delta\mathbf{q}(k+1)$ and $\Delta a_f(k+1)$ into the RAMAS and feed mechanism simultaneously, the state $\mathbf{s}_j$ at the next time step $(k+1)$ is expected to be obtained in two ways: from the simulation and real experimental platforms, respectively. In the simulation, forward kinematics mapping is leveraged to estimate state $\mathbf{s}_j(k+1)$ by integrating Eqs. (6) and (14):

$$\mathbf{s}_j(k+1) = F_{JT}(F_{AJ}(\mathbf{a}(k) + \Delta\mathbf{a}(k+1))). \tag{25}$$

By contrast, state $\mathbf{s}_j(k+1)$ is observed using a camera in an actual environment and can be described as

$$\mathbf{s}_j(k+1) = {}^{\mathcal{B}}_{\mathcal{O}}\mathbf{H}\ {}^{\mathcal{O}}\mathbf{s}_j(k+1) \tag{26}$$

where ${}^{\mathcal{B}}_{\mathcal{O}}\mathbf{H}$ transforms ${}^{\mathcal{O}}\mathbf{s}_j$ from the description in $\{\mathcal{O}\}$ to that in $\{\mathcal{B}\}$. The algorithm used to obtain ${}^{\mathcal{O}}\mathbf{s}_j(k+1)$ is shown in Fig. 6(c). Four labels (yellow) are marked lengthwise in order: two are labeled tightly at the distal end of the PBM, and the other two are labeled at the distal tip of the ABM. Thus, we denote the mapping C that obtains the states ${}^{\mathcal{O}}\mathbf{s}_j$ from the label positions as

$${}^{\mathcal{O}}\mathbf{s}_j(k+1) = C({}^{\mathcal{O}}p_{lix}(k+1), {}^{\mathcal{O}}p_{liy}(k+1)) \quad (i = 1, 2, 3, 4) \tag{27}$$

where ${}^{\mathcal{O}}p_{lix}(k)$ and ${}^{\mathcal{O}}p_{liy}(k)$ are the projections of the four markers on the x and y axes of $\{\mathcal{O}\}$, respectively. Thus, we have $\Delta\mathbf{s}_j(k+2) = \mathbf{s}_j^* - \mathbf{s}_j(k+1)$ for the next iteration until the convergence.

The second mode achieves global shape control. The global shape includes the orientation angle of the (N_p)th link γ_{N_p2}, orientation angle of tip link γ_{N2}, and position p_{Nx}. So, we define the robot state $\mathbf{s}_j \in \mathbb{R}^3$ as

$$\mathbf{s}_j(k) = [\gamma_{N_p2}(k),\ \gamma_{N2}(k),\ p_{Nx}(k)]^T. \tag{28}$$

Moreover, the control mapping for the second mode M_2 is given by

$$\Delta\mathbf{a}(k+1) = M_2(\mathbf{a}(k), \Delta\mathbf{s}_j(k+1)). \tag{29}$$

B. NN Based Controller Design

Because optimization exists during forward kinematics modeling and the mapping expressions from the actuation space to the task space are not completely analytical, we attempted to adopt data-driven approaches to construct the two mappings M_1 and M_2. Data-driven approaches have attracted much interest in the field of robot control because complex model relationships are not necessary and the convenience

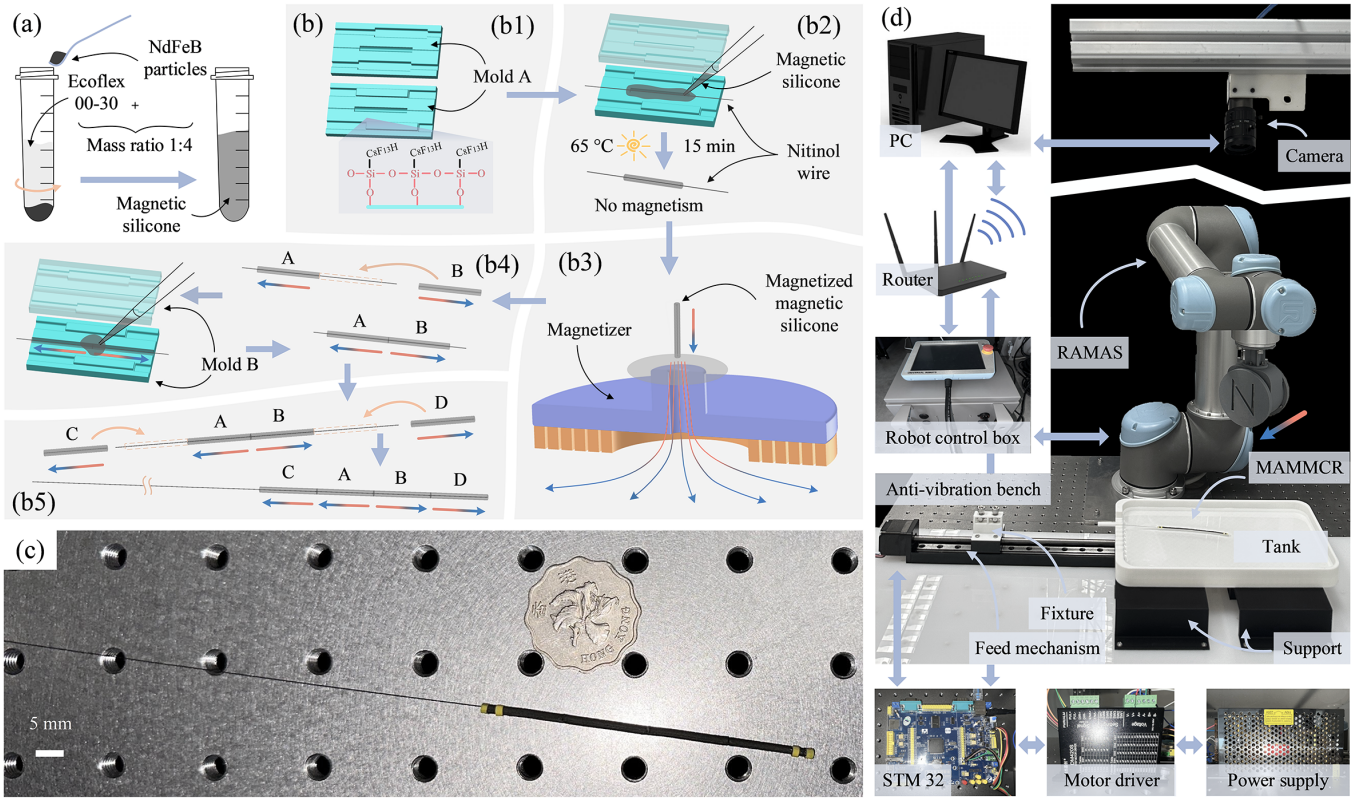

Fig. 7. Fabrication of the robot prototype and construction of the validation setup. (a) Preparation of the magnetic silicone. (b) Fabrication of the prototype via the prepared magnetic silicone: (b1) Molds after the hydrophobic treatment. (b2) Molding of ABM segments. (b3) Magnetization process. (b4) Connecting of two adjacent ABM segments. (b5) Assembly of all prototype parts. (c) MAMMCR prototype. Four attached yellow labels were designed for the visual detection. (d) Overview of the validation setup. The hardware system includes the MAMMCR, tank, feed mechanism, RAMAS, camera, and other components that connect and make the system function together, such as the PC, router, and robot control box. The blue arrows show the mutual connection of these system components.

TABLE III
NN TRAINING PARAMETERS

Aspect	Parameter	Value [Unit]
Architecture	Layer number	8
	Layer neuron number	128 × 256 × 512 × 1024 × 2048 × 512 × 256 × 128
Data exploration	p_{mx}	-80-240 [mm]
	p_{my}	150-300 [mm]
	β_{m2}	-180-180 [°]
	a_f	0-80 [mm]
	δp_{mx}	10 [mm]
	δp_{my}	10 [mm]
	$\delta \beta_{m2}$	5 [°]
	δa_f	10 [mm]
Training	Batch size	512
	Maximum epoch number	30000
	Early stop number	2000
	Maximum learning rate	0.001
	Momentum	0.7
	Weight decay	0.0001

of fast computation [50]–[53]. Therefore, two NN-based controllers were designed and trained in a supervised manner to approximate the two mappings (Fig. 6(d)).

The parameters used in NN construction and training are listed in Table III. For convenience, the two NNs shared the identical initial architecture but were trained independently. This was reasonable, considering that equal amounts of training and validation data were fed to each network during the training process. Therefore, they did not share network parameters and each network obtained its determinate parameters individually. The constructed NN architecture consisted of eight hidden layers, with the number of neurons in each layer following a pyramid pattern of initially increasing and then decreasing.

For the training data, data pairs, including the input parts, $\mathbf{a}$ and $\Delta \mathbf{s}_j$, and the output part, $\Delta \mathbf{a}$, were sampled via data exploration in the actuating space shown in Fig. 6(e1). The data pairs were obtained via the forward kinematics modeling derived in this study for convenient and fast data collection. Here, $\mathbf{a}_m$ is sampled in a square region. The projections of $\mathbf{p}_m$ on the x- and y-axes of $\{\mathcal{B}\}$, denoted as p_{mx} and p_{my}, underwent changes in the ranges of -80–240 mm and 150–300 mm with steps of 10 mm, respectively. β_{m2} underwent changes in the range of -180–180° in 90° intervals. Moreover, a_f spanned in the range of 0–80 mm in increments of 20 mm. Subsequently, for each sampled actuating vector $\mathbf{a}$, we provided a fluctuation vector $\Delta \mathbf{a}$ corresponding to each part of $\mathbf{a}$ under four scenarios or their combinations shown in Fig. 6(e2)–(e5), where δp_{mx}, δp_{my}, and δa_f were all set to 10

mm, and $\delta\beta_{m2}$ was set to 5°. Thus, given a set of samples $\mathbf{a}$ and $\Delta\mathbf{a}$, we can further obtain $\Delta\mathbf{s}_j$ to form a complete labeled data pair via Eq. (25). As a result, $\sim$ 620,000 sets of training data were collected.

Model training and validation were conducted on a laptop with a 12th Gen Intel Core 12900H CPU and an NVIDIA GeForce RTX 3070Ti GPU (8 GB memory). The hyperparameters used in the training procedure are listed in Table III. Specifically, stochastic gradient descent optimization algorithm accounted for iterative updates of the model parameters [26]. The iterative process continued until convergence to an optimal set of parameters that best fit the sampled training data. In addition, several training strategies were used to optimize and improve the model performance, including batch normalization, early stopping, momentum, and weight decay. Note that a special learning rate scheduling method, cosine annealing with warm starts, was leveraged to enable better convergence and potential escape from poor local minima by periodically decreasing the learning rate in a cosine-shaped manner and then resetting it to its initial value (Fig. 6(g)).

The results are presented as the average mean square errors (MSEs) of M_1 and M_2 on the validation set reach their minimum values of 3.817 in the 339th epoch and 3.678 in the 387th epoch. Beyond these two epochs, the training loss continued to gradually decrease, whereas the validation loss no longer decreased. Thus, the model parameters corresponding to the minimum average MSEs in the validation set were selected as the final model parameters (Fig. 6(f)). Note that the computing speed of our trained models during real-time tracking was much higher than those in existing studies [31], [37]. The mean computation time for learnt controllers during each iteration was $\sim 5 \times 10^{-6}$ ms, which indicates significant potential in real-time control.

C. Validation Setup

Fig. 7(d) shows an overview of the validation system. The entire setup was placed on an antivibration bench, and it primarily contained the MAMMCR, RAMAS, feed mechanism, camera, and other components that connected the main parts of the system, such as the PC, router, STM32 controller, motor driver, and power supply.

The MAMMCR was expected to navigate and deform in a 3D printed tank full with a glycerol aqueous solution (60% volume glycerol) under feed motion and a programmable magnetic field generated by the RAMAS. The liquid medium aided in simulating the human liquid environment, counteracting the robot's gravity, and reducing friction between the robot and its surroundings. The nitinol wire of the MAMMCR was fixed to the sliding platform of the feed mechanism using a homemade fixture. A permanent magnet (N52, dimensions: $\phi 68 \times 62.4$ mm^2) was adopted as the end-effector for the RAMAS, and the real time control of the RAMAS was built upon the Robot Operating System (ROS) on Ubuntu Linux.

V. Validations and Results

The deformability of our proposed MAMMCR and the effectiveness of the corresponding control algorithms were verified using both simulation and experimental platforms described in the aforementioned control framework. The robot was expected to navigate and deform under the two designed control modes. The core controllers of the two mappings M_1 and M_2 were obtained in an off-line learning fashion mentioned in the previous section.

TABLE IV
Initialization of Actuating Parameters

Actuating modules	Parameter	Initialization Value [Unit]
RAMAS	p_{mx}	80 [mm]
	p_{my}	300 [mm]
	$\mathbf{q}$	[0 -90 -115 -17 -90 -180] [°]
Feed mechanism	a_f	0 [mm]

A. Robot Prototype Fabrication

The prototype adopted a magnetically enhanced silicone with a much higher magnetic particle proportion (80% weight) than the existing MCRs (Table I). First, the silicone matrix (Ecoflex 00-30, with Parts A and B mixed in a 1:1 mass ratio) was obtained. The NdFeB particles (size: 5 μm) and silicone matrix were mixed in a 4:1 mass ratio (Fig. 7(a)). At this ratio, the mixture could simultaneously ensure high magnetism of the cured magnetic silicone and good fluidity for successful molding processes.

Before molding, we performed a hydrophobic treatment to graft perfluorohydrocarbon chains onto the resin surface of mold pairs 3D printed using a photosensitive resin and an ultraviolet printer (NOVA3D) (Fig. 7(b1)). Thus, the magnetic silicone injected into the mold cavities could be completely cured without impediments. The four segments of the ABM were molded using mold pair A and a pre-placed nitinol wire with a diameter of 0.2 mm ensured the center of the hollow cavity of the magnetic silicone segment (Fig. 7(b2)). The cured segments with no magnetism were then magnetized with an axial magnetization orientation using a magnetizer (Fig. 7(b3)). We assembled these axially magnetized segments along the nitinol wire to program MPC3 (Fig. 7(b4)). The adjacent segments were joined together after the second molding using the mold pair B. The fabricated prototype is shown in Fig. 7(c).

B. Control of MAMMCR Tip Position and Orientation

The control performance of mode M_1 was tested using target tracking under two scenarios. For the first scenario (Fig. 8(a)), the MAMMCR was controlled to track the contour of a four-leaf clover, where the tracking direction was labeled with light gray arrows. The entire contour was discretized into 96 points (red points), and the robot tip scanned each point sequentially while maintaining orientation angle γ_{N2} of 0 (red arrows) at each point. All the actuating parameters were initialized according to the values listed in Table IV. To reduce the influence of the RAMAS on the robot before the tracking task, we initialized the magnet from a safe distance (p_{my} =300 mm) away from the robot.

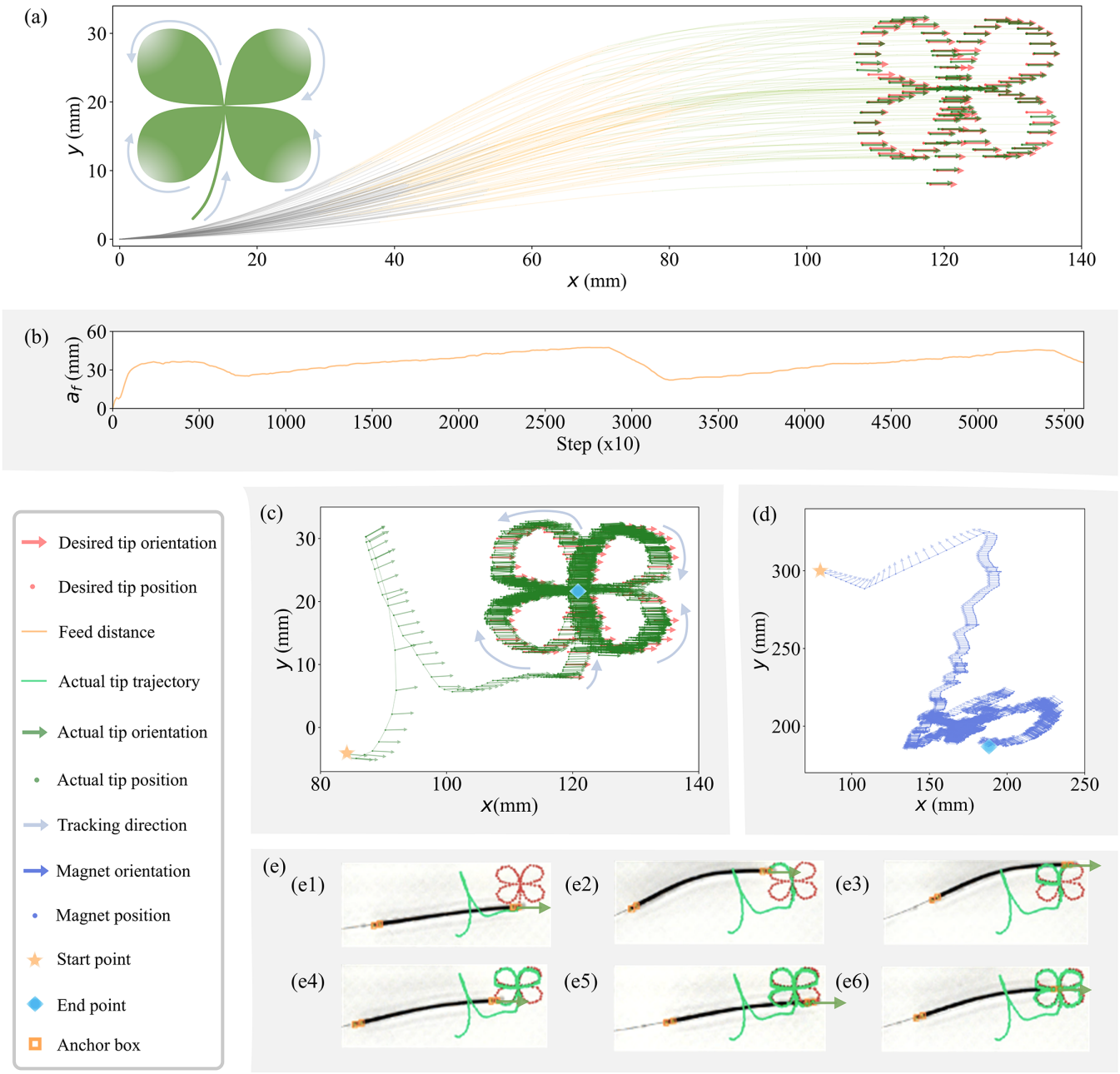

Fig. 8. Demonstration of the four-leaf clover tracking under the control mode M_1. (a) Discretized state trajectory obtained from the prepared path planning. At each point, the desired γ_{N2} is set as 0. Moreover, the converged deformation curve and states obtained from simulation at each discretized point are labeled. (b)–(e) Experimental results during the tracking: (b) Variations in the feed distance a_f. (c) State trajectory. (d) Motion trajectory of the external magnet. (e1)–(e6) Real time tracking under the visual feedback via the experimental setup.

First, we studied the control performance of the proposed algorithms in a simulation platform. The tracked tip points (green points) and the corresponding tip orientations (green arrows) after each convergence to the desired state are shown in Fig. 8(a). The real-time tracking process and state trajectory are shown in Supplementary Video S1 and Fig. S4(a), respectively. The feed motion and magnet trajectory during the tracking are shown in Supplementary Figs. S4(b) and (c), respectively. Regarding tracking performance, we analyzed the variations in three states, p_{Nx}, p_{Ny}, and γ_{N2}, and corresponding errors (Supplementary Fig. S6). MAEs of three states were 0.251 mm, 0.169 mm, and 0.246°, respectively. To evaluate error fluctuations, we determined the root MSEs of the three states as 0.343 mm, 0.235 mm, and 0.382°. With the designed algorithms, the magnet in the RAMAS seamlessly adjusted its position and orientation, enabling continuous motion of the robot tip and smooth variations in the tip orientation. We performed this demonstration using an experimental platform. The real-time tracking process is shown in Supplementary Video S1 and Figs. 8(b)–(e). In the error analyses (Supplementary Fig. S9), we observed the MAEs (and root MSEs) for the three states were 0.441 (0.608) mm, 0.254 (0.340) mm,

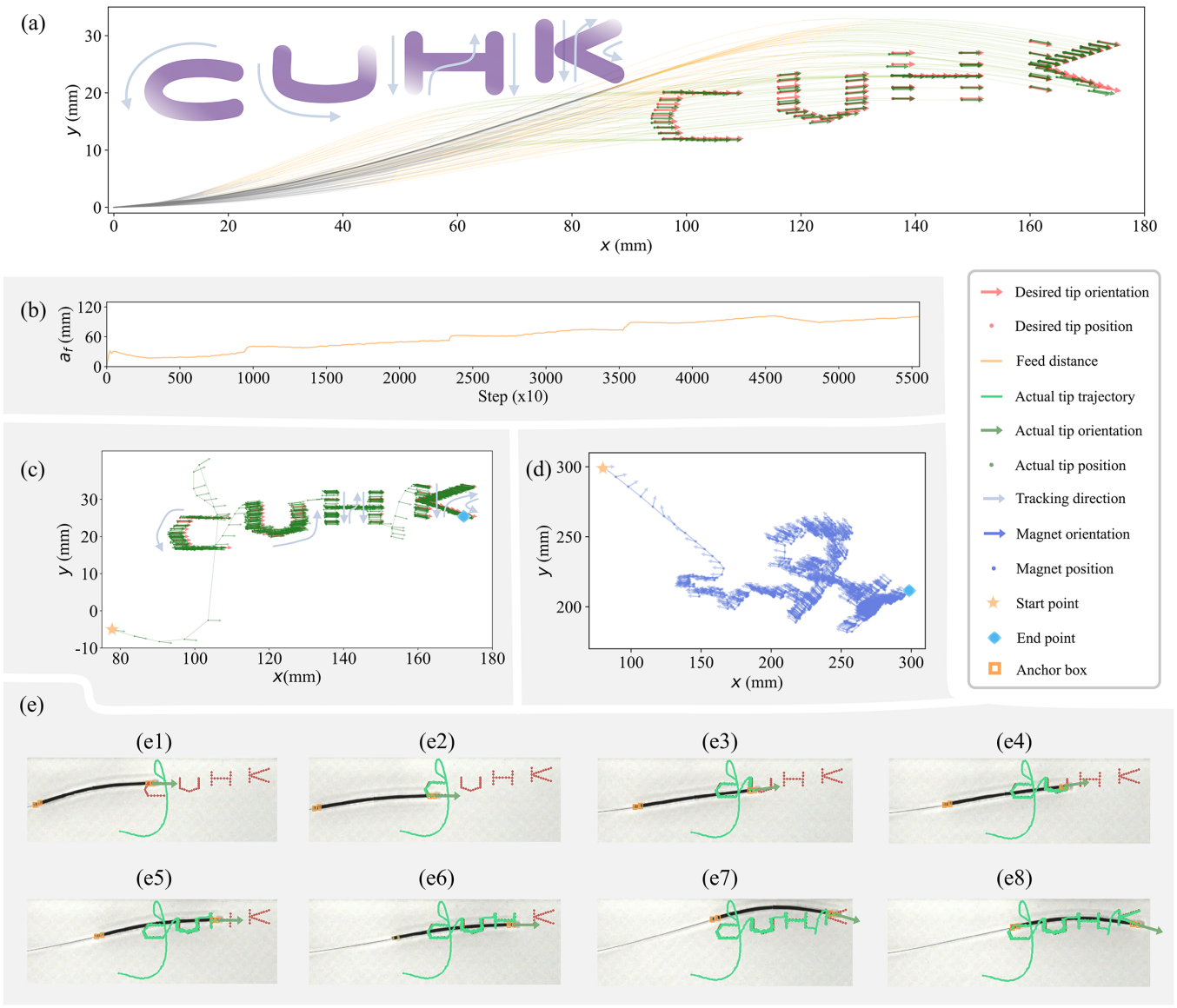

Fig. 9. Demonstration of the letter combination "CUHK" tracking under the control mode M_1. (a) Discretized state trajectory obtained from the prepared path planning. The desired γ_{N2} values of points in "C," "U," "H," and "K" were set as 0°, 5°, 0°, and -10°, respectively. Moreover, the converged deformation curve and states obtained from simulation at each discretized point were labeled. (b)–(e) Experimental results during the tracking: (b) Variations in the feed distance a_f. (c) State trajectory. (d) Motion trajectory of the external magnet. (e1)–(e6) Real time tracking under the visual feedback via the experimental setup.

and 0.626 (1.001)°, respectively.

In the second scenario, the MAMMCR was controlled to track a letter combination "CUHK" arranged in a tilted manner (Fig. 9(a)). "CUHK" was discretized into 90 points. Unlike in the first scenario, we expected the robot tip to maintain different specific orientations when tracking different letters. The desired γ_{N2} values of discretized points in "C," "U," "H," and "K" were set as 0°, 5°, 0°, and -10°, respectively. The actuating parameters were initialized in the same manner.

The real-time tracking process, state trajectory, magnet motion, and feed motion obtained from the simulation are shown in Supplementary Video S2 and Figs. S5(a)–(c), respectively. Based on the variations in the three controlled states and errors (Supplementary Fig. S7), the MAEs (and root MSEs) for the three states were 0.209 (0.281) mm, 0.198 (0.267) mm, and 0.192 (0.257)°, respectively. The experimental validation results, including the real-time tracking process and error analyses, are shown in Supplementary Video S2, Figs. 9(b)–(e), and Supplementary Fig. S10. The MAEs (and root MSEs) for the controlled states were 0.448 (0.591) mm, 0.280 (0.390) mm, and 0.807° (1.086°), respectively.

C. Control of MAMMCR Global Shape

We tested the control performance of the robot using the mode M_2. Here, the robot was expected to accurately tune the global shape, determined by γ_{N_p2}, γ_{N2}, and p_{Nx} during navigation. As shown in Fig. 10(a), the robot continuously modulated its shape while maintaining the tip along the lines of $x = 100$ mm. The tracking direction of the robot is

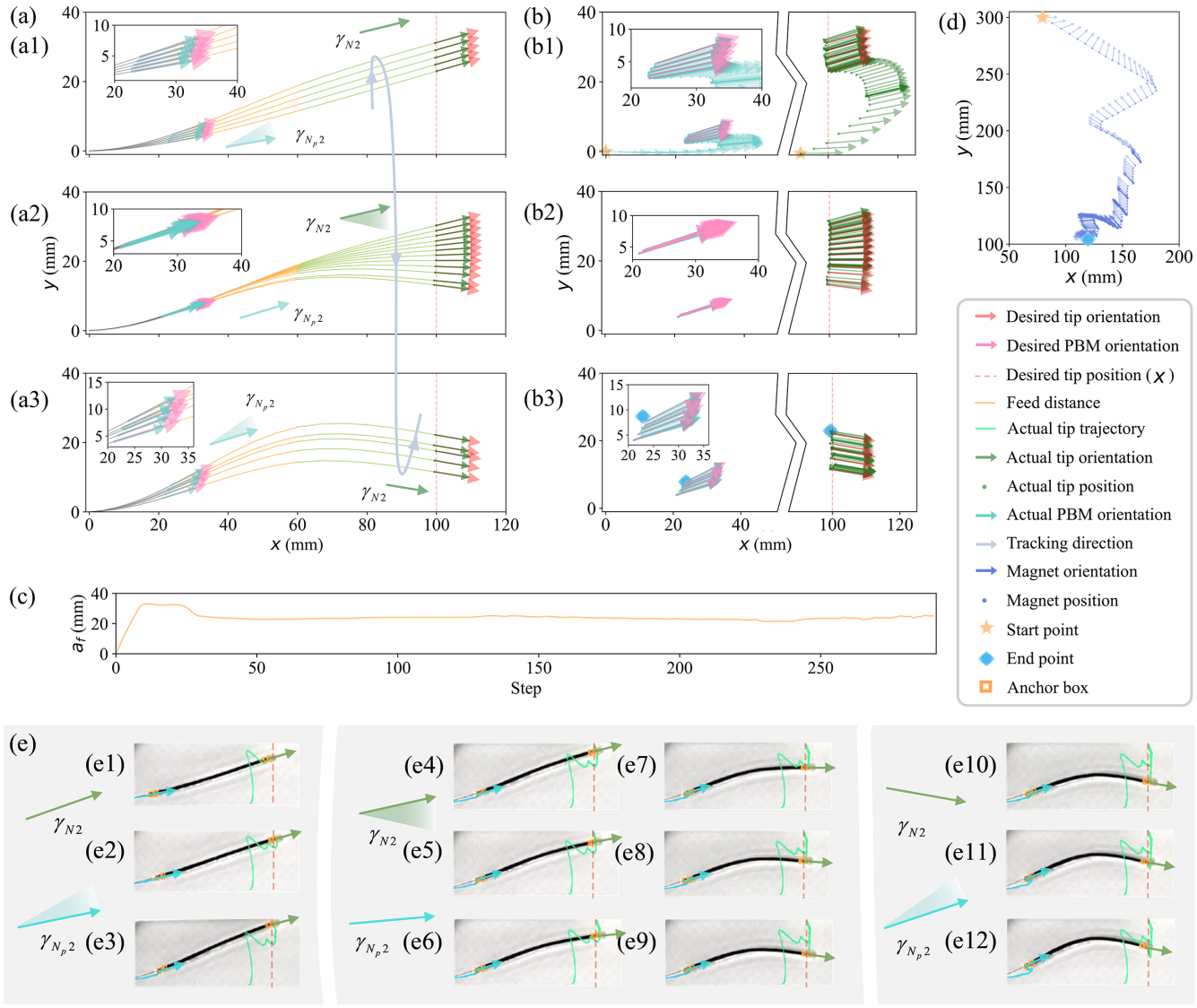

Fig. 10. Demonstration of the global shape tracking under the control mode M_2. (a) Discretized state trajectories. The desired state p_{Nx} is 100 mm: (a1) Desired state γ_{N2} remained at 16°, and the desired state γ_{N_p2} increased from 10 to 18° with increments of 2°; (a2) Desired state γ_{N_p2} remained at 18°, and the desired state γ_{N2} decreased from 14° to -8° with increments of -2°; (a3) Desired state γ_{N2} remained at -10°, and the desired state γ_{N_p2} increased from 18 to 26° with increments of 2°. (b)–(d): Simulation results during the tracking: (b) State trajectories of the robot, and (b1)–(b3) correspond to (a1)–(a3), respectively. (c) Variations in the feed distance a_f. (d) Motion trajectory of the external magnet. (e) Experimental results during the tracking: (e1)–(e3) Real-time tracking when the desired state γ_{N2} remained at 16°, and the desired state γ_{N_p2} were 10°, 14°, 18°, respectively; (e4)–(e9) Real-time tracking when the desired state γ_{N_p2} remained at 18°, and the desired state γ_{N2} were 14°, 10°, 6°, 0°, -4°, -8°, respectively; (e10)–(e12) Real-time tracking when the desired state γ_{N2} remained at -10°, and the desired state γ_{N_p2} are 18°, 22°, 26°, respectively.

indicated by light gray arrows. As shown in Fig. 10(a1), γ_{N2} was anticipated to remain constant at 16°, whereas γ_{N_p2} progressively increased from 10° to 18° in 2° increments. As shown in Fig. 10(a2), γ_{N_p2} was maintained at a fixed value of 18°, whereas γ_{N2} decreases from 14° to -8° with decrements of 2°. As shown in Fig. 10(a3), γ_{N2} maintained a constant value of -10°, whereas γ_{N2} continued to increase from 18° to 26° in 2° increments.

The simulation data of the real-time tracking process, state trajectories, feed motion, and magnet motion are shown in Supplementary Video S3 and Figs. 10(b)–(d), respectively. Regarding the observations of the three states and the corresponding errors (Supplementary Fig. S8), the MAEs (and root MSEs) for the three states were 0.431° (0.646°), 0.257° (0.458°), and 0.269 (0.354) mm, respectively. We observed that during shape tracking, the three states were controlled accurately to smoothly tune the deformation curves between the C and S shapes. In addition, during shape tracking, the robot tip was controlled to move in a line simultaneously as desired. Additionally, the demonstration was validated using an experimental platform. The experimental results of the tracking process and error analysis are shown in Supplementary Video S3, Fig. 10(e), and Supplementary Fig. S11. The MAEs (and root MSEs) for the three states were 0.086° (0.099°), 0.086° (0.100°), and 1.564 (1.695) mm, respectively. The discrepancies between the simulation and experimental

TABLE V
NOMENCLATURE

N_s, N, N_p, N_a	Segment number; total link number; link numbers in each segment of the PBM and ABM.
$\{\mathcal{C}_i\}, \{\mathcal{B}\}, \{\mathcal{R}\}, \{\mathcal{O}\}$	Reference frames located at the ith flexible joint, proximal base, base of the robotic arm, and camera base, respectively.
$\boldsymbol{\theta}, \boldsymbol{\theta}_i, \theta_{i1}, \theta_{i2}, \theta_{i3}$	MAMMCR joint configuration; rotation vector of the ith flexible joint; three angles that determine the bending plane, bending angle, and twisting of the ith link, respectively.
$\mathbf{p}_i, p_{ix}, p_{iy}, \mathbf{p}_m, p_{mx}, p_{my},$ $\delta p_{mx}, \delta p_{my}, p_{tix}, p_{tiy}$	Position of the ith flexible joint; projections of $\mathbf{p}_i$ on the x- and y-axes; position of the external magnet dipole; projections of $\mathbf{p}_m$ on the x- and y-axes; small fluctuations of p_{mx} and p_{my}; projections of the ith label on the x- and y-axes, respectively.
l_i, L_s, L_m	Length of the ith link; length of the ABM including all the N_s segments; length of the actuating magnet.
$a_f, \Delta a_f, \delta a_f$	Feed motion; increment of a_f; small fluctuation of a_f.
${}^{\mathcal{B}}_{\mathcal{C}_i}\mathbf{H}(\boldsymbol{\theta}), {}^{\mathcal{B}}_{\mathcal{C}_i}\mathbf{R}_i(\boldsymbol{\theta})$	Homogeneous transformation matrix describing the pose of $\{\mathcal{C}_i\}$; rotation matrix of $\{\mathcal{C}_i\}$.
$F_{JT}(.), F_{AJ}(.), M_i(.),$ $C(.)$	Joint-to-task space mapping; actuation-to-task space mapping; control mappings from the current state increment to the actuation increment for ith control mode; mapping from the label positions to controlled states of two modes.
$\boldsymbol{\xi}_{jk}$	Twist coordinate corresponding to the skew-symmetric matrix form $\hat{\boldsymbol{\xi}}_{jk}$.
$\overline{\boldsymbol{\omega}}_{jk}$	Rotation axis of the jth joint associated with the bending plane $(k=1)$, bending angle $(k=2)$, and twisting $(k=3)$.
$\mathbf{t}, \mathbf{t}_i$	Full task space vector; state of ith link, including the position and orientation of the link tip.
$\boldsymbol{\gamma}_i, \gamma_{i1}, \gamma_{i2}$	Angle vector of the ith link; two angles describing the tip orientation of the ith link.
$\overline{\mathbf{o}}_i, \overline{\mathbf{o}}_m$	Unit vector describing the orientation of the ith link; orientation of the external magnet dipole.
$\mathbf{m}_m, \mathbf{m}_i, m_m, m_i, m_p$	Magnetic moment vectors of the external magnet dipole and the ith link; strengths of $\mathbf{m}_m$ and $\mathbf{m}_i$; magnetic moment strength of the magnetic particles per unit mass.
$\mathbf{B}_i, B_r$	Magnetic field exerted on the ith link; magnet remanence.
μ_0	Vacuum permeability.
D_m, D_a, D_p	Diameters of the actuating magnet, ABM, and PBM.
χ	Mass ratio of magnetic particles in the magnetic silicone.
M_p	Magnetic moment strength of the magnetic particles per unit mass.
$\rho_{ms}, \rho_p, \rho_s$	Densities of the magnetic silicone, magnetic particles, and silicone.
$\mathbf{W}, \overline{\mathbf{w}}_i, \mathbf{w}_+, \mathbf{w}_-$	Magnetization profile configuration of the MAMMCR; unit vector describing the magnetization orientation of the ith link; magnetization vectors for ABM segments with $+x$ or $-x$ magnetization.
$\mathbf{a}, \mathbf{a}_m, \Delta\mathbf{a}, \Delta\mathbf{a}_m$	Actuating vector; magnetic actuating vector; increments of $\mathbf{a}$ and $\mathbf{a}_m$.
$\boldsymbol{\beta}_m, \beta_{m1}, \beta_{m2}, \delta\beta_{m2}$	Angle vector of the magnet dipole; Angle swept by rotating from the z-axis to $\overline{\mathbf{o}}_m$; angle swept by rotating from the x-axis to the vector obtained by projecting $\overline{\mathbf{o}}_m$ onto the x-y plane; small variation of β_{m2}.
$\mathbf{d}_i, \mathbf{d}_{ji}$	Vector from the magnet position $\mathbf{p}_m$ to the geometrical center of the ith link; vector from the center of the jth link to that of the ith link.
V_E, V_B, V_G	Strain energy, magnetic potential energy, and gravitational potential energy of the robot.
K_i, T_i	Bending stiffness and torsional stiffness of the ith link.
G_i	Gravity of the ith link.
$\boldsymbol{\lambda}_z, \boldsymbol{\lambda}_d, \lambda_1, \lambda_2$	Coefficient matrix extracting the coordinate value in the z-direction of $\mathbf{p}_i$; damping coefficient matrix; damping coefficient of the magnet position; damping coefficient of the magnet orientation.
τ_c, τ_h	Deformabilities of the MAMMCR under the C and S or higher-order shapes.
i_p	Link number: the link angle reaches the first non-zero extremum value when the robot deforms into an S or higher-order shapes.
$S^*, s_j^*, s_j, \Delta s_j$	Sequence of controlled states of the MAMMCR for ith control mode; jth ground truth of a desired robot state of sequence $\mathbf{S}^*$; controlled state of the MAMMCR for ith control mode corresponding to $\mathbf{s}_j^*$; increment of $\mathbf{s}_j$.
$\mathbf{q}, \Delta\mathbf{q}$	Joint vector of the robotic arm in the RAMAS; increment of $\mathbf{q}$.
$\mathbf{J}, \mathbf{J}_d$	Jacobian matrix of the robotic arm; damped Jacobian of the robotic arm.

errors were primarily due to the inaccuracies of the model, such as ignoring the friction between the liquid and our robot during tracking, assembly errors among different parts of the entire setup, and calibration errors of the intrinsic and extrinsic parameters of the camera. Although a slightly inferior convergence performance of the p_{Nx} experimental results was exhibited compared with the simulations, the accurate tracking of the robot shapes ensured and demonstrated the effectiveness of the algorithms and good control performance of our robot.

VI. CONCLUSION

In this study, we propose methodologies for designing and controlling an MAMMCR. First, a static PRB model and an index-based deformability evaluation strategy are introduced to analyze the deformability of robots with different MPCs. Based on the optimized MPC, the kinematic behavior of the robot is numerically characterized. A control framework with two learnt controllers is devised to endow the robot with two control modes: tip and global shape controls. The two controllers approximate the mapping from the tip pose or global shape to the actuation increments. They were trained with data generated using the PRB model and demonstrated a high performance in terms of the computation time and accuracy. Finally, a fabrication method is proposed, and three case demonstrations were performed via simulation and experimental platforms to validate the good deformability of the robot and the effectiveness of the algorithms. The experimental results showed the best control performance with MAEs of 0.254 mm and 0.626° for mode M_1 and 1.564 mm and 0.086° for mode M_2. This may provide our robot more potential of

TABLE VI
ACRONYMS

ABM	Active bending module.
CR	Continuum robot.
DoF	Degree of Freedom.
MAE	Mean absolute error.
MAMMCR	Modular axially magnetized magnetic continuum robot.
MCR	Magnetic continuum robot.
MIS	Minimally invasive surgery.
MPC	Magnetization profile configuration.
MSE	Mean square error.
NN	Neural network.
PBM	Passive bending module.
PRB	Pseudo rigid body.
RAMAS	Robotic arm-based magnetic actuating system.
ROS	Robot Operating System.

navigation in body cavities or organs to perform ablation or palpation in the future.

Future research should consider developing an online-learning error compensator in the control framework to further improve the tracking performance of the robot. Additionally, we will consider feedback mechanisms other than visual detection, such as fiber Bragg gratings and ultrasound. This endows our robot and control system with a greater potential for *ex vivo* or *in vivo* applications.

APPENDIX A
NOMENCLATURE

All the symbols, variables, and their explanations defined in this paper are listed in Table V.

APPENDIX B
ACRONYMS

The abbreviations introduced in this paper can be alphabetically tracked in a glossary (Table VI).

REFERENCES

[1] M. Runciman, A. Darzi, G. P. Mylonas, "Soft robotics in minimally invasive surgery," *Soft Robot.*, vol. 6, no. 4, pp. 423–443, 2019.

[2] A. Zemmar, A. M. Lozano, B. J. Nelson, "The rise of robots in surgical environments during COVID-19," *Nat. Mach. Intell.*, vol. 2, no. 10, pp. 566–572, 2020.

[3] M. Cai, Z. Qi, Y. Cao, X. Liu, X. Wu, T. Xu, L. Zhang. Venkiteswaran, S. Misra, "Performance-Guided Rotating Magnetic Field Control in Large Workspaces with Reconfigurable Electromagnetic Actuation System," *IEEE Trans. Robot.*, vol. 40, pp. 4117–4131, 2024.

[4] P. E. Dupont, B. J. Nelson, M. Goldfarb, B. Hannaford, A. Menciassi, M. K. O'Malley, N. Simaan, P. Valdastri, G. Z. Yang, "A decade retrospective of medical robotics research from 2010 to 2020," *Sci. Robot.*, vol. 6, no. 60, 2021, Art. no. eabi8017.

[5] J. Burgner-Kahrs, D. C. Rucker, H. Choset, "Continuum robots for medical applications: A survey," *IEEE Trans. Robot.*, vol. 31, no. 6, pp. 1261–1280, 2015.

[6] T. da Veiga, J. H. Chandler, P. Lloyd, G. Pittiglio, N. J Wilkinson, A. K. Hoshiar, R. A. Harris, P. Valdastri, "Challenges of continuum robots in clinical context: A review," *Prog. Biomed. Eng.*, vol. 2, no. 3, 2020, Art. no. 032003.

[7] Q. Peyron, Q. Boehler, P. Rougeot, P. Roux, B. J. Nelson, N. Andreff, K. Rabenorosoa, P. Renaud, "Magnetic concentric tube robots: Introduction and analysis," *Int. J. Robot. Res.*, vol. 41, no. 4, pp. 418–440, 2022.

[8] A. Gao, R. R. Murphy, W. Chen, G. Dagnino, P. Fischer, M. G. Gutierrez, D. Kundrat, B. J. Nelson, N. Shamsudhin, H. Su, J, Xia, A. Zemmar, D. Zhang, C. Wang, G. Z. Yang, "Progress in robotics for combating infectious diseases," *Sci. Robot.*, vol. 6, no. 52, 2021, Art. no. eabf1462.

[9] H. Guo, F. Ju, Y. Cao, F. Qi, D. Bai, Y. Wang, B. Chen, "Continuum robot shape estimation using permanent magnets and magnetic sensors," *Sens. Actuators A Phys.*, vol. 285, pp. 519–530, 2019.

[10] C. Yang, S. Geng, I. Walker, D. T. Branson, J. Liu, J. S. Dai, R. Kang, "Geometric constraintbased modeling and analysis of a novel continuum robot with shape memory alloy initiated variable stiffness," *Int. J. Robot. Res.*, vol. 39, no. 14, pp. 1620–1634, 2020.

[11] Y. Cao, F. Ju, L. Zhang, D. Bai, F. Qi, B. Chen, "A novel variable-stiffness flexible manipulator actuated by shape memory alloy for minimally invasive surgery," *Proc. Inst. Mech. Eng. H*, vol. 232, no. 11, pp. 1098–1110, 2018.

[12] W. Liu, Y. Duo, J. Liu, F. Yuan, L. Li, L. Li, G. Wang, B. Chen, S. Wang, H. Yang, Y. Liu, Y. Mo, Y. Wang, B. Fang, F. Sun, X. Ding, C. Zhang, L. Wen, "Touchless interactive teaching of soft robots through flexible bimodal sensory interfaces," *Nat. Commun.*, vol. 13, no. 1, pp. 1–14, 2022.

[13] G. M. Elena, "Novel design of a soft lightweight pneumatic continuum robot arm with decoupled variable stiffness and positioning," *Soft Robot.*, vol. 5, no. 1, pp. 54–70, 2018.

[14] Z. Dong, X. Wang, G. Fang, Z. He, J. D. L. Ho, C. L. Cheung, W. L. Tang, X. Xie, L. Liang, H. C. Chang, C. K. Ching, K. W. Kwok, "Shape tracking and feedback control of cardiac catheter using MRI-guided robotic platform—Validation with pulmonary vein isolation simulator in MRI," *IEEE Trans. Robot.*, vol. 38, no. 5, pp. 2781–2798, 2022.

[15] K. H. Lee, K. C. D. Fu, Z. Guo, Z. Dong, M. C. W. Leong, C. L. Cheung, A. P. W. Lee, W. Luk, K. W. Kwok, "MR safe robotic manipulator for MRI-guided intracardiac catheterization," *IEEE/ASME Trans. Mechatron.*, vol. 23, no. 2, pp. 586–595, 2018.

[16] D. C. Rucker, B. A. Jones, R. J. Webster III, "A geometrically exact model for externally loaded concentric-tube continuum robots," *IEEE Trans. Robot.*, vol. 26, no. 5, pp. 769–780, 2010.

[17] S. Lilge, J. Burgner-Kahrs, "Kinetostatic modeling of tendon-driven parallel continuum robots," *IEEE Trans. Robot.*, vol. 39, no. 2, pp. 1563–1579, 2022.

[18] B. J. Nelson, S. Gervasoni, P. W. Y. Chiu, L. Zhang, A. Zemmar, "Magnetically actuated medical robots: An in vivo perspective," *Proc. IEEE*, vol. 100, no. 7, pp. 1028–1037, 2022.

[19] Z. Yang, H. Yang, Y. Cao, Y. Cui, L. Zhang, "Magnetically Actuated Continuum Medical Robots: A Review," *Adv. Intell. Syst.*, 2023, Art. no. 2200416.

[20] X. Yang, W. Shang, H. Lu, Y Liu, L Yang, R Tan, X Wu, Y Shen, "An agglutinate magnetic spray transforms inanimate objects into millirobots for biomedical applications," *Sci. Robot.*, vol. 5, no. 48, 2020, Art. no. eabc8191.

[21] Z. Yang, L. Zhang, "Magnetic actuation systems for miniature robots: A review," *Adv. Intell. Syst.*, vol. 2, no. 9, 2020, Art. no. 2000082.

[22] M. Cai, Z. Qi, Y. Cao, X. Wu, T. Xu, L. Zhang, "Development of Reconfigurable Electromagnetic Actuation System With Large Workspaces: Design, Optimization, and Validation," *IEEE Trans. Autom. Sci. Eng.*, 2024.

[23] H. Gu, M. Möckli, C. Ehmke, M. Kim, M. Wieland, S. Moser, C. Bechinger, Q. Boehler, B. J. Nelson "Self-folding soft-robotic chains with reconfigurable shapes and functionalities," *Nat. Commun.*, vol. 14, no. 1, 2023, Art. no. 1263.

[24] M. Cai, Z. Qi, Y. Cao, X. Wu, T. Xu, L. Zhang, "Magnetic Field-Priority Force Control for Automated Manipulation in Large Workspaces With Reconfigurable Electromagnetic Actuation System," *IEEE Trans. Ind. Electron.*, 2024.

[25] B. Sun, M. Sun, Z. Zhang, Y. Jiang B. Hao, X. Wang, Y. Cao, T. K. F. Chan, L. Zhang, "Magnetic Hydrogel Micromachines with Active Release of Antibacterial Agent for Biofilm Eradication," *Adv. Intell. Syst.*, vol. 14, no. 1, 2023, Art. no. 2300092.

[26] M. Cai, Q. Wang, Z. Qi, D. Jin, X. Wu, T. Xu, L. Zhang, "Deep Reinforcement Learning Framework-Based Flow Rate Rejection Control of Soft Magnetic Miniature Robots," *IEEE Trans. Cybern.*, 2022.

[27] S. Jeon, A. K. Hoshiar, K. Kim, S. Lee, E. Kim, S. Lee, J. Kim, B. J. Nelson, H. J. Cha, B. J. Yi, H. Choi, "A magnetically controlled soft microrobot steering a guidewire in a threedimensional phantom vascular network," *Soft Robot.*, vol. 6, no. 1, pp. 54–68, 2019.

[28] Z. Yang, L. Yang, M. Zhang, C. Zhang, S. C. H. Yu, L. Zhang, "Ultrasound-guided catheterization using a driller-tipped guidewire with

combined magnetic navigation and drilling motion," *IEEE ASME Trans. Mechatron.*, vol. 27, no. 5, pp. 2829–2840, 2021.
[29] W. Lee, J. Nam, J. Kim, E. Jung, N. Kim, G. Jang, "Steering, tunneling, and stent delivery of a multifunctional magnetic catheter robot to treat occlusive vascular disease," *IEEE Trans. Ind. Electron.*, vol. 68, no. 1, pp. 391–400, 2020.
[30] Z. Yang, L. Yang, M. Zhang, Q. Wang, S. C. H. Yu, L. Zhang, "Magnetic control of a steerable guidewire under ultrasound guidance using mobile electromagnets," *IEEE Robot. Autom. Lett.*, vol. 6, no. 2, pp. 1280–1287, 2021.
[31] J. Edelmann, A. J. Petruska, B. J. Nelson, "Magnetic control of continuum devices," *Int. J. Robot. Res.*, vol. 36, no. 1, pp. 68–85, 2017.
[32] J. Sikorski, C. M. Heunis, R. Obeid, V. K. Venkiteswaran, S. Misra, "A flexible catheter system for ultrasound-guided magnetic projectile delivery," *IEEE Trans. Robot.*, vol. 38, no. 3, pp. 1959–1972, 2021.
[33] Z. Yang, L. Yang, M. Zhang, N. Xia, L. Zhang, "Ultrasound-guided wired magnetic microrobot with active steering and ejectable tip," *IEEE Trans. Ind. Electron.*, vol. 70, no. 1, pp. 614–623, 2022.
[34] Y. Kim, E. Genevriere, P. Harker, J. Choe, M. Balicki, R. W. Regenhardt, J. E. Vranic, A. A. Dmytriw, A. B. Patel, X. Zhao, "Telerobotic neurovascular interventions with magnetic manipulation," *Sci. Robot.*, vol. 7, no. 65, 2022, Art. no. eabg9907.
[35] J. Hwang, S. Jeon, B. Kim, J. Y. Kim, C. Jin, A. Yeon, B. J. Yi, C. H. Yoon, H. J. Park, S. Pane, B. J. Nelson, H. Choi, "An Electromagnetically Controllable Microrobotic Interventional System for Targeted, Real-Time Cardiovascular Intervention," *Adv. Healthc. Mater.*, vol. 11, no. 11, 2022, Art. no. 2102529.
[36] Y. Kim, G. A. Parada, S. Liu, X. Zhao, "Ferromagnetic soft continuum robots," *Sci. Robot.*, vol. 4, no. 33, 2022, Art. no. eaax7329.
[37] D. Lin, W. Chen, K. He, N. Jiao, Z. Wang, L. Liu, "Position and orientation control of multisection magnetic soft microcatheters," *IEEE ASME Trans. Mechatron.*, vol. 28, no. 2, pp. 907–918, 2022.
[38] D. Lin, N. Jiao, Z. Wang, L. Liu, "A magnetic continuum robot with multi-mode control using opposite-magnetized magnets," *IEEE Robot. Autom. Lett.*, vol. 6, no. 2, pp. 2485–2492, 2021.
[39] Y. Cao, Z. Yang, B. Hao, X. Wang, M. Cai, Z. Qi, B. Sun, Q. Wang, L. Zhang, "Magnetic Continuum Robot with Intraoperative Magnetic Moment Programming," *Soft Robot.*, 2023.
[40] J. Xue, M. Zhang, X. Liu, J. Zhu, Y. Cao, L. Zhang, "A Magnetic Continuum Robot with In-situ Magnetic Reprogramming Capability," *IEEE In. Conf. Robot. Autom.*, pp. 5891–5897, 2024.
[41] G. Pittiglio, P. Lloyd, T. da Veiga, O. Onaizah, C. Pompili, J. H. Chandler, P. Valdastri, "Patient-specific magnetic catheters for atraumatic autonomous endoscopy," *Soft Robot.*, vol. 57, no. 16, pp. 4258–4273, 2022.
[42] L. Wang, D. Zheng, P. Harker, A. B. Patel, C. F. Guo, X. Zhao, "Evolutionary design of magnetic soft continuum robots," *Proc. Natl. Acad. Sci. U S A*, vol. 118, no. 21, 2021, Art. no. e2021922118.
[43] G. Z. Lum, Z. Ye, X. Dong, H. Marvi, O. Erin, W. Hu, M. Sitti, "Shape-programmable magnetic soft matter," *Proc. Natl. Acad. Sci. U S A*, vol. 113, no. 41, pp. E6007–E6015, 2016.
[44] P. Lloyd, A. K. Hoshiar, T. da Veiga, A. Attanasio, N. Marahrens, J. H. Chandler, P. Valdastri, "A learnt approach for the design of magnetically actuated shape forming soft tentacle robots," *IEEE Robot. Autom. Lett.*, vol. 5, no. 3, pp. 3937–3944, 2020.
[45] G. Pittiglio, A. L. Orekhov, T. da Veiga, S Calò, J. H. Chandler, N. Marahrens, P. Valdastri, "Closed loop static control of multi-magnet soft continuum robots," *IEEE Robot. Autom. Lett.*, 2023.
[46] M. Richter, V. K. Venkiteswaran, S. Misra, "Multi-point orientation control of discretely-magnetized continuum manipulators," *IEEE Robot. Autom. Lett.*, vol. 6, no. 2, pp. 3607-3614, 2021.
[47] Y. Ni, Y. Sun, H. Zhang, X. Li, S. Zhang, M. Li, "Data-driven navigation of ferromagnetic soft continuum robots based on machine learning," *Adv. Intell. Syst.*, vol. 5, no. 2, 2023, Art. no. 2200167.
[48] J. Sikorski, A. Denasi, G. Bucchi, S. Scheggi, S. Misra, "Vision-based 3-D control of magnetically actuated catheter using BigMag—An array of mobile electromagnetic coils," *IEEE ASME Trans. Mechatron.*, vol. 24, no. 2, pp. 505-516, 2019.
[49] X. Yang, L. Wu, J. Li, K. Chen, "A minimal kinematic model for serial robot calibration using POE formula," *Robot. Comput. Integr. Manuf.*, vol. 30, no. 3, pp. 326-334, 2014.
[50] X. Wang, Y. Li, K. W. Kwok, "A survey for machine learning-based control of continuum robots," *Front. Robot. AI*, vol. 24, 2021, Art. no. 730330.
[51] Y. Ni, Y. Sun, H. Zhang, X. Li, S. Zhang, M. Li, "Data-Driven Navigation of Ferromagnetic Soft Continuum Robots Based on Machine Learning," *Adv. Intell. Syst.*, vol. 5, no. 2, 2023, Art. no. 2200167.
[52] T. G. Thuruthel, E. Falotico, F. Renda, C. Laschi, "Model-based reinforcement learning for closed-loop dynamic control of soft robotic manipulators," *IEEE Trans. Robot.*, vol. 35, no. 1, pp. 124-134, 2018.
[53] X. Wang, J. Dai, H. S. Tong, K. Wang, G. Fang, X. Xie, Y. H. Liu, K. W. S. Au, K. W. Kwok, "Learning-Based Visual-Strain Fusion for Eye-in-Hand Continuum Robot Pose Estimation and Control," *IEEE Trans. Robot.*, 2023.

Yanfei Cao (Graduate Student Member, IEEE) received his B.E. degree in mechanical engineering and automation and the M.E. degree in mechanical and electronic engineering from the Nanjing University of Aeronautics and Astronautics, China, in 2016 and 2019, respectively. He is currently a Ph.D. candidate and working towards the Ph.D. degree in mechanical and automation engineering with The Chinese University of Hong Kong, Hong Kong, China.

His research interests include continuum robots, magnetic materials and actuation, and learning-based control.

Mingxue Cai (Member, IEEE) received the Ph.D. degree in control theory and control engineering from the Institute of Automation, Chinese Academy of Sciences, Beijing, China, in 2020.

He was a Postdoctoral Fellow with The Chinese University of Hong Kong from 2021 to 2023. He is currently an Associate Professor with the Shenzhen Institutes of Advanced Technology, Chinese Academy of Sciences, Shenzhen, China. His current research interests include robotics, intelligent control, deep reinforcement learning.

Bonan Sun received both bachelor's and master's degrees in Engineering Mechanics from Xi'an Jiaotong University. He is currently a PhD candidate in Mechanical and Automation Engineering at The Chinese University of Hong Kong.

His research interests include microrobots, soft robots, hydrogels, biofilms, and soft matter mechanics.

Zhaoyang Qi (Graduate Student Member, IEEE) received the bachelor's degree in instrument science and technology from the Hefei University of Technology, Hefei, China, in 2018, and master's degree in instrument science and technology from the University of Science and Technology of China, Hefei, China, in 2021. He is currently working toward the Ph.D. degree in mechanical and automation engineering with The Chinese University of Hong Kong, Hong Kong, China.

His research interests include intelligent control of medical robotics.

Junnan Xue (Graduate Student Member, IEEE) received the B.E. degree in mechanical and electronic engineering from the Taiyuan University of Technology, Taiyuan, China, in 2020, and the M.E. degree in mechanical engineering from the Harbin Institute of Technology, Shenzhen, China, in 2022. He is currently working toward the Ph.D. degree in mechanical and automation engineering with The Chinese University of Hong Kong, Hong Kong.

His research interests include medical robotics and small-scale robotics.

Yihang Jiang received the B.Eng. degree in Biomedical Engineering from Henan University of Science and Technology, Luoyang, China, in 2017, and the M.Eng. degree in Biomedical Engineering from Shenzhen University, Shenzhen, China, in 2022. He is currently pursuing a Ph.D. degree in Mechanical Automation Engineering at The Chinese University of Hong Kong (CUHK).

His research interests focus on microrobotics for biomedical applications.

Bo Hao received the B.S. degree in aircraft design and engineering from Nanjing University of Aeronautics and Astronautics, Nanjing, China, in 2016, the M.S. degree in mechanical and aeronautical engineering from the École Nationale Supérieure de Mécanique et d'Aérotechnique, Poitiers, France, in 2019, and the M.E. degree in mechanical engineering from Nanjing University of Aeronautics and Astronautics, in 2020. He is currently pursuing the Ph.D. degree with the Chinese University of Hong Kong, Hong Kong, China.

His research interest includes small-scale robotics.

Jiaqi Zhu received the B.S. degree in mechanical design manufacture and automation from the Yanshan University, Qinhuangdao, China, in 2019, and the M.S. degree in mechanical engineering from Huazhong University of Science and Technology, Wuhan, China, in 2022. He is currently working toward the Ph.D. degree in Mechanical and Automation Engineering with The Chinese University of Hong Kong.

His research interests include small scale medical robot, soft-rigid hybrid machines, and stretchable electronics.

Xurui Liu received the bachelor's degree in optoelectronic information science and engineering from Harbin Institute of Technology, Weihai, China, in 2018, and the master's degree in microelectronics and solid state electronics from Huazhong University of Science and Technology, Wuhan, China, in 2022. He is currently pursuing the Ph.D. degree with the Department of Mechanical and Automation Engineering, The Chinese University of Hong Kong, Hong Kong, China.

His research interests include miniature machines and sensors for biomedical applications.

Chaoyu Yang received his B.S. and Ph.D. degrees in Engineering from the University of Science and Technology of China (USTC) in 2015 and 2020, respectively. After completing his Ph.D., he served as a Postdoctoral Fellow at the Wenzhou Institute, University of the Chinese Academy of Sciences (UCAS).

He is currently a Research Assistant Professor in the Department of Mechanical and Automation Engineering at The Chinese University of Hong Kong (CUHK). His research specializes in advanced materials for microfluidics and their applications.

Li Zhang (Fellow, IEEE) received the Ph.D. degree in physics from the University of Basel, Basel, Switzerland, in 2007.

He is currently a Professor with the Department of Mechanical and Automation Engineering and a Professor by Courtesy with the Department of Surgery, The Chinese University of Hong Kong, Hong Kong. His research interests include miniature robots and their biomedical applications.